On the Superposition of Mean Advective and Eddy-Induced Transports in Global Ocean Heat and Salt Budgets

FABIO BOEIRA DIAS,[a,b,c,d] C. M. DOMINGUES,[a,c,d] S. J. MARSLAND,[b,c,d,a] S. M. GRIFFIES,[e,f] S. R. RINTOUL,[b,d] R. MATEAR,[b] AND R. FIEDLER[b]

[a] *Institute for Marine and Antarctic Studies, University of Tasmania, Hobart, Tasmania, Australia*
[b] *CSIRO Oceans and Atmosphere, Aspendale, Victoria, Australia*
[c] *ARC Centre of Excellence for Climate Extremes, University of Tasmania, Hobart, Tasmania, Australia*
[d] *Antarctic Climate and Ecosystem Cooperative Research Centre, Hobart, Tasmania, Australia*
[e] *NOAA/Geophysical Fluid Dynamics Laboratory, Princeton, New Jersey*
[f] *Program in Atmospheric and Ocean Sciences, Princeton University, Princeton, New Jersey*

(Manuscript received 6 June 2019, in final form 11 October 2019)

ABSTRACT

Ocean thermal expansion is a large contributor to observed sea level rise, which is expected to continue into the future. However, large uncertainties exist in sea level projections among climate models, partially due to intermodel differences in ocean heat uptake and redistribution of buoyancy. Here, the mechanisms of vertical ocean heat and salt transport are investigated in quasi-steady-state model simulations using the Australian Community Climate and Earth-System Simulator Ocean Model (ACCESS-OM2). New insights into the net effect of key physical processes are gained within the superresidual transport (SRT) framework. In this framework, vertical tracer transport is dominated by downward fluxes associated with the large-scale ocean circulation and upward fluxes induced by mesoscale eddies, with two distinct physical regimes. In the upper ocean, where high-latitude water masses are formed by mixed layer processes, through cooling or salinification, the SRT counteracts those processes by transporting heat and salt downward. In contrast, in the ocean interior, the SRT opposes dianeutral diffusion via upward fluxes of heat and salt, with about 60% of the vertical heat transport occurring in the Southern Ocean. Overall, the SRT is largely responsible for removing newly formed water masses from the mixed layer into the ocean interior, where they are eroded by dianeutral diffusion. Unlike the classical advective–diffusive balance, dianeutral diffusion is bottom intensified above rough bottom topography, allowing an overturning cell to develop in alignment with recent theories. Implications are discussed for understanding the role of vertical tracer transport on the simulation of ocean climate and sea level.

1. Introduction

The oceans play a major role in the climate system by absorbing about 93% of the additional heat accumulated over the 1971–2010 period (Rhein et al. 2013). As a result, the global ocean has slowed down the rate of global surface atmospheric warming (Otto et al. 2013) associated with emissions of anthropogenic greenhouse gases (Le Quéré et al. 2015). Through thermal expansion of the ocean's volume, increasing global ocean heat content (GOHC) has contributed about one-third of the global mean sea level (GMSL) rise observed since 1970 (Rhein et al. 2013) and is expected to continue into the future (Church et al. 2013).

Sea level rise projections from phase 5 of the latest Coupled Model Intercomparison Project (CMIP5) have a large spread at global and regional scales, partly caused by differences in ocean heat uptake (affecting ocean density) and redistribution by ocean circulation processes (Kuhlbrodt and Gregory 2012). Based on the multimodel ensemble mean, thermosteric mean sea level accounts for 30%–50% of the global mean sea level rise over the twenty-first century (Gregory et al. 2016), while spread in the ensemble of regional sea level is about 30% of the rate of GMSL rise in a moderate RCP4.5 emission scenario (e.g., Bouttes and Gregory 2014).

Denotes content that is immediately available upon publication as open access.

Corresponding author: Fabio Boeira Dias, fabio.dias@utas.edu.au

DOI: 10.1175/JCLI-D-19-0418.1

Progress in reducing uncertainty in sea level projections has been slow, in part due to a lack of model diagnostics for a mechanistic understanding of ocean processes (Gregory et al. 2016). With greater international collaboration and coordination, as well as computer power and storage capacity, there is now an opportunity to systematically quantify the key ocean processes controlling ocean density (heat and salt) and circulation changes in CMIP-type model simulations. Gregory et al. (2016) designed an experimental protocol to specifically address process-based model analyses of ocean heat uptake and transport—the Flux-Anomaly-Forced Model Intercomparison Project (FAFMIP)—as part of CMIP6 (Eyring et al. 2016). FAFMIP's required diagnostics are detailed in the CMIP6 Ocean Model Intercomparison Project (OMIP) (Griffies et al. 2016).

To date, only a few quantitative analyses have examined the role of physical processes in the global ocean heat and salt balances. In the mean state, Gregory (2000), Gnanadesikan et al. (2005), Wolfe et al. (2008), Hieronymus and Nycander (2013), and Kuhlbrodt et al. (2015) found a different global vertical balance than the advective–diffusive balance proposed by Munk (1966). Munk's abyssal recipe follows the theory of Stommel and Arons (1960), where the steady-state overturning circulation is explained by a slow and uniformly distributed upwelling of cold waters (originating in high latitudes) balanced by a constant downward small-scale diffusion (mixing) throughout the ocean interior (Kuhlbrodt et al. 2007).

Gregory (2000) was the first to show that the global heat balance in a climate model is dominated by downward transport due to the wind-driven mean circulation (mean advection) and upward diffusive transport along isopycnals (isoneutral diffusion) in the Southern Ocean. Further studies showed that not only isoneutral diffusion (or eddy diffusion) but also eddy advection plays a role in the upward heat transport. The importance of these processes was demonstrated in eddy-resolving and eddy-permitting models (Wolfe et al. 2008; Kuhlbrodt et al. 2015; Griffies et al. 2015; von Storch et al. 2016) and in coarse-resolution models using the Gent and McWilliams (1990) eddy parameterization (Gnanadesikan et al. 2005; Hieronymus and Nycander 2013).

A residual mean theory has been described for the Southern Ocean meridional overturning circulation (Marshall and Radko 2003), where the downward transport by mean advection is offset by upward transport from eddy advection. Kuhlbrodt et al. (2015), based on results from an eddy-permitting climate model, found a balance between isoneutral diffusion and this residual mean for most of the ocean interior—a ''superresidual'' transport comprising the effect of mean advection and both eddy diffusion and eddy advection, although no conclusion about the role of the superresidual transport in the heat budget was made. This superresidual transport framework allows for direct model intercomparisons, as it overcomes differences in the combined representation of those three processes depending on model resolution. For example, some eddy-permitting models include a parameterization for isoneutral diffusion (Megann et al. 2014; Kuhlbrodt et al. 2015) whereas some others consider that the resolved advection induces sufficient isopycnal mixing (Wolfe et al. 2008; Morrison et al. 2013; Griffies et al. 2015; von Storch et al. 2016).

In this study, we use a budget analysis to examine the role of the superresidual transport in the global vertical balance of heat and salt under a quasi-steady state, including regional distribution of key processes involved and their depth dependency. Our results are based on a model simulation using the Australian Community Climate and Earth-System Simulator Ocean Model ocean–sea ice version 2.0 (ACCESS-OM2) (Bi et al. 2013; Kiss et al. 2019), forced with the JRA55-do dataset (Tsujino et al. 2018).

This paper is organized as follows: Section 2 describes the ACCESS-OM2 configuration, the Japanese 55-year Reanalysis driving ocean (JRA55-do) surface flux products, and the experimental design. Section 3 explains the budget approach. Budget results for the global mean state are found in section 4 and the regional contributions are explored in section 5. The vertical distribution of the main processes is described in section 6. Discussion and conclusions are found in sections 7 and 8, respectively.

2. Ocean–sea ice model simulations

a. *ACCESS-OM2 configuration*

The global model used in this study is ACCESS-OM2. This version is largely based on the configuration described in Bi et al. (2013), with updates described in Kiss et al. (2019). These updates include the fifth version of the National Oceanic and Atmospheric Administration (NOAA) Geophysical Fluid Dynamics Laboratory (GFDL) Modular Ocean Model (MOM5) for the ocean component, the Los Alamos sea ice model (CICE), version 5 (Hunke et al. 2013), coupled with the Centre Européen de Recherche et de Formation Avancée en Calcul Scientifique Ocean Atmosphere Sea Ice Soil, version 3, with the Model Coupling Toolkit (OASIS3-MCT) from the Argonne National Laboratory (Valcke et al. 2015).

The ACCESS-OM2 ocean model makes use of a hydrostatic and Boussinesq form of the MOM5 of Griffies and Greatbatch (2012). Nominal horizontal resolution is 1°, with higher meridional resolution (1/3°) in an equatorial band, with cosine-dependent (Mercator) meridional

resolution in the Southern Ocean, and a tripolar grid in the Arctic following Murray (1996). In the vertical, the domain comprises 50 levels with z^* coordinates (Stacey et al. 1995; Adcroft et al. 1997) varying between 10 m of thickness near surface and 333 m in the abyssal ocean. To prevent unrealistic model states, a sea surface salinity restoring is applied with a time scale of 60 days over the upper layer with a nominal 10-m thickness [for a discussion on salinity restoring time scale, please see Danabasoglu et al. (2014)].

To represent the subgridscale processes, the model includes an isoneutral diffusion parameterization from Solomon (1971) and Redi (1982) as implemented by Griffies et al. (1998, hereafter G98), and a Gent and McWilliams (1990, hereafter GM90) scheme formulated as a skew flux (G98) as implemented according to Ferrari et al. (2010). The neutral diffusion scheme also includes a tapering scheme for large neutral slopes from Danabasoglu and McWilliams (1995). In the surface ocean boundary layer, the vertical mixing follows the K-profile parameterization (KPP) from Large et al. (1994), and in the mixed layer the restratification effects from baroclinic eddies are parameterized according to Fox-Kemper et al. (2011). Convective adjustment uses the parameterization from Klinger et al. (1996) through enhancement of dianeutral diffusion. In addition, the horizontal friction uses a Smagorinsky biharmonic scheme following Griffies and Hallberg (2000), a tidal mixing parameterization from Simmons et al. (2004), and the coastal tide mixing scheme of Lee et al. (2006). Dense waters moving into the abyssal ocean are parameterized with a downslope mixing scheme as described in Snow et al. (2015). The main subgridscale parameter coefficients used in our simulations are listed in Table 1.

Table 1. Coefficients used in subgridscale parameterizations: KPP (Large et al. 1994), tidal mixing scheme S04 (Simmons et al. 2004), isoneutral diffusion (G98), tapering of isoneutral diffusion DM95 (Danabasoglu and McWilliams 1995), and eddy advection (GM90; Ferrari and Ferreira 2011).

Parameter	Scheme	Value
Maximum viscosity due to shear instability	KPP	$5 \times 10^{-3}\ \mathrm{m^2\,s^{-1}}$
Maximum diffusivity due to shear instability	KPP	$5 \times 10^{-3}\ \mathrm{m^2\,s^{-1}}$
Viscosity due to convective instability	KPP	$0.1\ \mathrm{m^2\,s^{-1}}$
Diffusivity due to convective instability	KPP	$0.1\ \mathrm{m^2\,s^{-1}}$
Roughness scale	S04	12 000 m
Neutral diffusivity	G98	$600\ \mathrm{m^2\,s^{-1}}$
Maximum isoneutral slope	G98	0.01
Transition for scaling isoneutral diffusivities	DM95	0.004
Half-width scaling for diffusivity	DM95	0.001
Eddy-induced advection (skew) diffusivity: minimum to maximum range	GM90	50–600 $\mathrm{m^2\,s^{-1}}$

b. Surface forcing datasets

Our ACCESS-OM2 simulation was driven by the JRA55-do surface forcing product from Tsujino et al. (2018). The JRA55-do was developed based on JRA-55 (Kobayashi et al. 2015) from the Japan Meteorological Agency (JMA) to complement the previous widely used Co-ordinated Ocean–Ice Reference Experiments (CORE) product developed by Large and Yeager (2009), used in coordinated model intercomparisons (Griffies et al. 2009; Danabasoglu et al. 2014). The unavailability of CORE after 2009, along with its relatively low horizontal resolution, motivated the development of the JRA55-do product (Tsujino et al. 2018). The JRA55-do, version 1.3, provides atmospheric fields on a 55-km horizontal grid every 3 h from 1958 to 2018. Although JRA55-do's adjustment method to reference datasets is similar to CORE, refinements were introduced through the use of satellite and atmospheric reanalysis from other projects, with surface air temperature and specific humidity diagnostics relying on multireanalysis ensemble means (Tsujino et al. 2018).

Although there is not yet an official version for normal year forcing (NYF, equivalent to CORE-I), for this study, we adopted the repeated year 1984–85 [repeat year forcing (RYF)] with a start in May. This RYF showed the strongest Atlantic meridional overturning circulation (AMOC) and smallest salinity biases of those RYF tested (not shown). Starting the RYF in May (and ending in April) helps to reduce the transition across the year boundary, as the climatological monthly mean and variance of the climate indices are smaller during May in both hemispheres (K. Stewart 2018, personal communication).

c. Experimental design

The model was initialized with climatological potential temperature and practical salinity from the *World Ocean Atlas 2013* (*WOA13*; Zweng et al. 2013; Locarnini et al. 2013) and spun up for 1000 years (Fig. 1) to reach near thermodynamical equilibrium. Although this spinup is focused on the long-term response from the ocean–sea ice system (internal variability), it also retains synoptic variability (Griffies et al. 2009). We averaged the last 20 years of the spinup to obtain our annual mean state.

While ocean models usually show a relatively fast adjustment in the upper pycnocline region over about 50–100 years, the deep ocean can drift for centuries to millennia due to imbalances between the initial and boundary conditions, and/or biases in the simulated ocean circulation (Griffies et al. 2009). Our 1000-yr

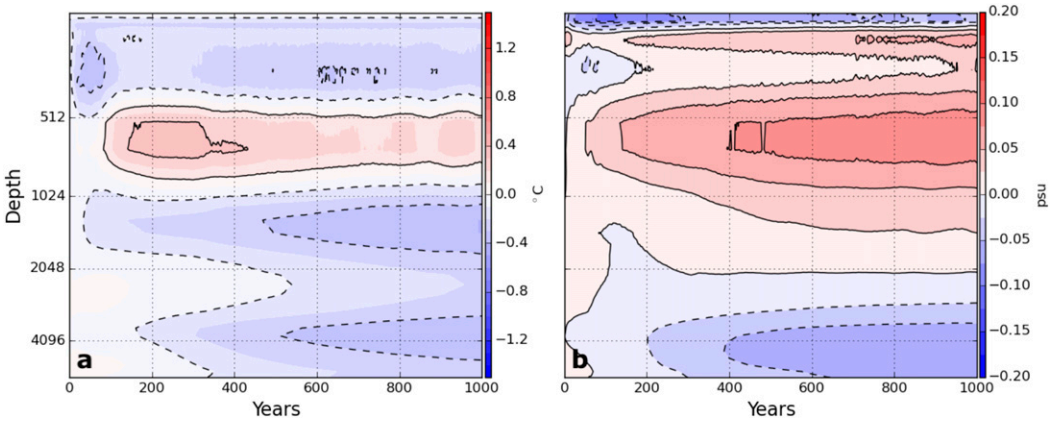

FIG. 1. Horizontally averaged drift (difference from model output relative to the *WOA13* climatology) of the annual mean (a) temperature (°C) and (b) salinity (psu) for JRA55-do RYF simulation. The depth axes are plotted in $\log_2$ for a clear view of the upper ocean. Contour lines are defined for 0.2°C intervals in (a) and 0.025-psu intervals in (b).

model integration greatly reduced drift in the deep ocean, with the meridional overturning, subtropical and subpolar gyres, convection, and deep-water formation reaching a near-steady state (not shown).

3. Ocean budget approach

To quantify processes responsible for temperature and salinity transport, we use a set of online tendency diagnostics (see Table 2 for a summary of all terms). The time tendency for the heat content in a grid cell, per unit horizontal area, can be written as

$$C_p \rho_0 \frac{\partial(\Theta\, dz)}{\partial t} = -\nabla_z \cdot \mathbf{F} - \delta_k \mathbf{F}^z, \tag{1}$$

where Θ is conservative temperature, ρ_0 is a reference density ($1035\,\mathrm{kg\,m^{-3}}$), and C_p is heat capacity ($3992\,\mathrm{J\,kg^{-1}\,°C}$). The time tendency for the heat content [lhs of Eq. (1)] results from the convergence of a variety of heat fluxes (rhs). The

TABLE 2. Details of the terms involved in the budget analysis.

Acronym	Term name	Summary	Diagnostic (heat)	Diagnostic (salt)
SFC	Surface fluxes	Dianeutral diffusion due to surface fluxes	temp_vdiffuse_sbc	salt_vdiffuse_sbc
ADV	Mean advection	Large-scale (resolved) advection	temp_advection	salt_advection
DIA	Dianeutral diffusion	Vertical turbulent diffusion (minus vertical convection) (minus surface fluxes)	temp_vdiffuse_impl -temp_vdiffuse_diff_cbt_conv -temp_vdiffuse_sbc	salt_vdiffuse_impl -salt_vdiffuse_diff_cbt_conv -salt_vdiffuse_sbc
KPP	Nonlocal KPP	Vertical mixing parameterization of the boundary layer	temp_nonlocal_KPP	salt_nonlocal_KPP
EIT	Eddy-induced transport	Parameterized eddy advection and neutral diffusion	neutral_gm_temp + neutral_diffusion_temp	neutral_gm_salt + neutral_diffusion_salt
SUB	Submesoscale eddies	Parameterized restratification from submesoscale eddies	temp_submeso	salt_submeso
CON	Convection	Vertical convection and downslope mixing	temp_vdiffuse_diff_cbt_conv + mixdownslope_temp	salt_vdiffuse_diff_cbt_conv + mixdownslope_salt
SWP	Shortwave penetration	Penetrative shortwave radiation	sw_heat	—
PME	Precipitation minus evaporation	Fluxes due to precipitation and evaporation exchange	sfc_hflux_pme	pme_sbc
RIV	River runoff	Fluxes due to river runoff	temp_rivermix	river
FRZ	Frazil	Flux due to frazil formation	frazil_3d	—
ICE	Ice flux	Ice flux	—	sfc_salt_flux_ice + melt
RES	Restore flux	Restoring salt flux	—	sfc_salt_flux_restore
SRT	Superresidual transport	Sum of resolved advection + mesoscale eddy-induced advection plus diffusion SRT = ADV + EIT	—	—

variety of heat fluxes **F** that can alter the heat content of a grid cell in ACCESS-OM2 are

$$\mathbf{F} = \mathrm{SFC} + \mathrm{ADV} + \mathrm{DIA} + \mathrm{KPP} + \mathrm{SWP} + \mathrm{EIT} + \mathrm{SUB} + \mathrm{CON} + \mathrm{PME} + \mathrm{RIV} + \mathrm{FRZ}. \quad (2)$$

Except for the net air–sea fluxes (SFC; only acting at the surface layer) and mean advection (ADV) terms, all other terms in the rhs of Eq. (2) are represented by subgridscale (SGS) processes:

- DIA: Dianeutral (across neutral surfaces) diffusion. The background diffusivity was configured with the latitudinal-dependent scheme from Jochum (2009), with a constant value outside the tropics (k_0 of $0.5 \times 10^{-5}\,\mathrm{m^2\,s^{-1}}$), reducing to $1 \times 10^{-6}\,\mathrm{m^2\,s^{-1}}$ at the equator (20°S–20°N). Various parameterizations affect the dianeutral diffusion, including tidal mixing, the local component of *K*-profile parameterization (shear instabilities, double diffusion), and convection (presented separately as CON, see below).
- KPP: The nonlocal component of the *K*-profile parameterization for the ocean surface boundary layer (OBL).
- SWP: Shortwave penetration through the water column.
- EIT: Eddy-induced transport, combined effect of parameterized eddy advection (GM90) and parameterized eddy (isoneutral) diffusion (G98).
- SUB: The restratification term from submesoscale eddies in the mixed layer.
- CON: Includes mixing due to convective instabilities [parameterized through enhancement of vertical diffusivity following Klinger et al. (1996)] and the overflow parameterization of dense water flowing down topographic slopes (downslope mixing scheme).
- PME/RIV: The mass flux at the surface due to real water flux boundary conditions carries heat content into and out of the ocean through the precipitation (liquid and solid) and evaporation (PME) and river runoff (RIV) terms. By convention, the heat content of mass exchanged across the ocean boundary is computed with respect to 0°C. Liquid and solid precipitation are assumed to have the same temperature as the ocean surface.
- FRZ: Formation of frazil sea ice when the temperature of seawater cools below the freezing point.

The salt budget in Eq. (3) is written in a manner similar to the heat budget in Eq. (1):

$$\rho_0 \frac{\partial (S\,dz)}{\partial t} = -\nabla_z \cdot \mathbf{F} - \delta_k \mathbf{F}^z, \quad (3)$$

with the fluxes **F** contributing to salinity changes in a grid cell given by

$$\mathbf{F} = \mathrm{SFC} + \mathrm{ADV} + \mathrm{DIA} + \mathrm{KPP} + \mathrm{EIT} + \mathrm{SUB} + \mathrm{CON} + \mathrm{ICE} + \mathrm{RES} + \mathrm{PME} + \mathrm{RIV}. \quad (4)$$

Compared to the heat fluxes in Eq. (2), the salt fluxes in Eq. (4) are not affected by SWP and FRZ and include two extra terms to account for surface salt fluxes due to sea surface salinity restoring (RES) and exchange with sea ice (ICE; see Table 2). For comparison with PME and RIV, we converted RES and ICE into equivalent freshwater fluxes. As our model simulation conserves ocean heat and salt within each grid cell, the sum of the rhs terms (transport convergence) is equal to the lhs (tracer tendency) in Eqs. (1) and (3).

4. Global balance

The globally integrated drift in annual mean temperature and salinity (Fig. 1) over the final several hundred years of the simulation is small relative to that from the previous generation of models in Griffies et al. (2009, their Figs. 5 and 6). Relative to the *WOA13* climatology (Locarnini et al. 2013), the temperature evolution shows a mild cooling (>−0.4°C) in the upper 500 m, a warming tendency between 500 and 800 m, less than 0.2°C, associated with Subantarctic Mode Water (SAMW) and Antarctic Intermediate Water (AAIW), and a general cooling below 800 m, associated with North Atlantic Deep Water (NADW) and Antarctic Bottom Water (AABW). Changes in the salinity (Zweng et al. 2013) show a freshening (negative bias) over the surface layer and deep ocean below 2000 m while positive biases occur from subsurface to 2000 m.

The 20-yr mean state of the global vertical transport for each physical process listed in Table 2 is shown in Fig. 2. Downward (upward) transport of heat or salt is denoted by positive (negative) fluxes. The net tendency (NET; lhs of the budget equations) is close to zero (black line) as expected for a quasi-steady state. The processes that control the vertical transport below 200 m are basically the same for heat and salt but as expected they differ considerably in the upper 200 m, where the effect of different surface heat and salt/freshwater boundary fluxes are most pronounced. Model temperature and salinity drifts (Fig. 1) are negligible to the interpretation of the budgets (at least one order of magnitude smaller than the transport due to individual processes).

In the upper 100 m, the vertical heat transport arises from the balance between downward heat fluxes due to DIA along with SWP and upward heat fluxes from the nonlocal vertical mixing (KPP) and CON (Fig. 2). Other terms have secondary importance. For the salt budget, DIA is balanced by all the other processes in the top 200 m (Fig. 2) but this

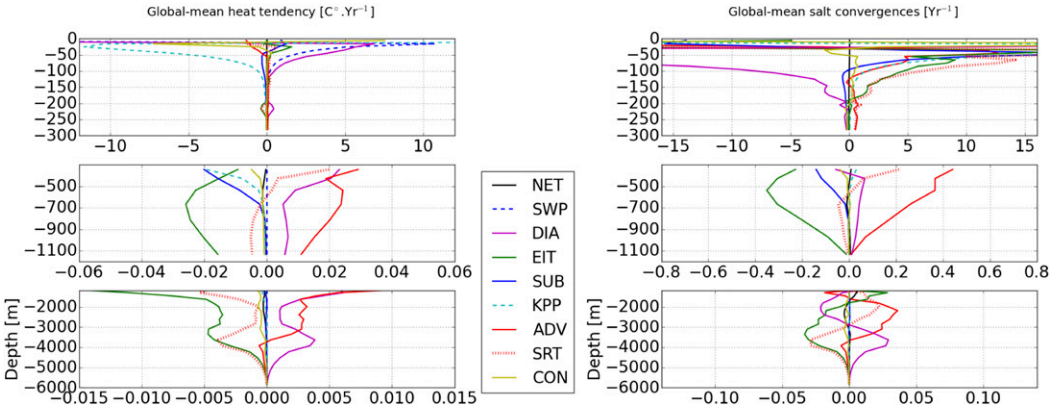

FIG. 2. Global (horizontally integrated) ocean (left) heat and (right) salt budgets for the mean state. Budget terms [rhs in Eqs. (1) and (3)] are listed in Table 2. Their sum is equivalent to the net tendency [black line; lhs in Eqs. (1) and (3)]. Flux units are °C yr^{-1} for heat and yr^{-1} for salt. Note the different limits in the x axis for different depth intervals. Positive (negative) is downward (upward) flux for both heat and salt.

balance varies over depth, where strong salinity gradients in the pycnocline exist. In the top 50 m, DIA represents mixed layer processes and drives a downward salt flux. Below 50 m, DIA results in upward salt flux. The relationship between the upper-700-m processes and surface fluxes is investigated in section 5a.

Below 200 m, vertical transport results from the same balance of physical processes for heat and salt (Fig. 2). The largest transport convergences are explained by the ADV and EIT, down to 3500 m. The EIT accounts for eddy-induced advection (GM90) and isoneutral diffusion (G98), with similar contributions to the upward transport. As in previous studies, upward transport by EIT is balanced by downward transport due to ADV in the mean state (e.g., Hieronymus and Nycander 2013; Kuhlbrodt et al. 2015; Griffies et al. 2015; von Storch et al. 2016).

As both components of EIT (eddy-induced advection and isoneutral diffusion) can be seen as diffusive processes on isopycnals, they can be added to the large-scale advection ADV to result in a "superresidual" transport (SRT), as defined by Kuhlbrodt et al. (2015):

$$\mathrm{SRT} = \mathrm{ADV} + \mathrm{EIT}. \tag{5}$$

This term was originally proposed as a novel way to examine the residual advection (ADV + GM parameterization part of the EIT) balanced with mixing along neutral surfaces (isoneutral or eddy diffusion) below 200 m. Here, we found that the SRT has two depth-dependent regimes for both heat and salt—hereafter "upper ocean" and "ocean interior"—roughly separated at 700–800 m in the global integral (Fig. 2). Above 700–800 m, including deep mixed layers in high latitudes, downward SRT flux is compensated by upward fluxes from convection, nonlocal KPP, and SUB. Below 700–800 m, the upward SRT flux is balanced by downward flux via DIA. We do not include the submesoscale scheme in the SRT as we focus on that portion of the parameterized flow that is largely associated with geostrophic flow, such as from the GM90 and G98 schemes. In contrast, the Fox-Kemper et al. (2011) scheme is associated with order-1 Rossby number baroclinic eddies in the mixed layer (Boccaletti et al. 2007). As SUB has similar effect and depth distribution to the nonlocal KPP, these processes are combined in the analyses of section 6.

Several studies have highlighted the importance of eddy fluxes in compensating the downward transport of large-scale advection (e.g., Wolfe et al. 2008; Griffies et al. 2015; von Storch et al. 2016; Saenko et al. 2018), but no study so far has discussed the role of the SRT after being introduced by Kuhlbrodt et al. (2015). In the next sections, we will show that the two global-integral SRT regimes (sections 5a and 5b) identified above are linked with regional formation and redistribution of dense water masses (SAMW, AAIW, NADW, and AABW) by effectively removing recently formed dense water from deep mixed layer regions into the ocean interior (section 6). We suggest that the SRT mechanism in the ocean interior regime can be reinterpreted as the advective part of the classical advective–diffusive balance of Stommel and Arons (1960) and Munk (1966), although not uniformly distributed in the deep and abyssal ocean. In this new perspective, our SRT results differ from the similar studies mentioned above, where Munk's balance was deemed to have only a minor role in their global heat and salt budgets (Hieronymus and Nycander 2013; Kuhlbrodt et al. 2015).

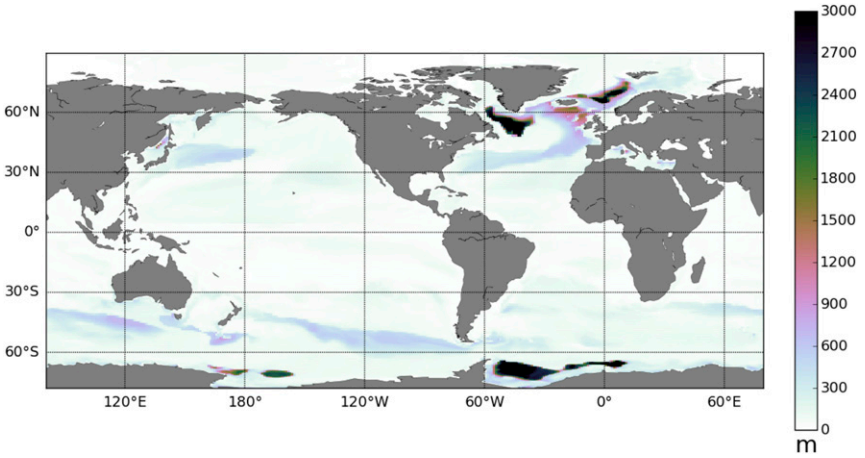

FIG. 3. Winter mixed layer depth (MLD) for the mean state of the JRA55 RYF experiment. The threshold criteria used to diagnose the MLD follows Danabasoglu et al. (2014) for the Northern Hemisphere (March; depth at which the potential density changes by 0.125 kg m^{-3} from its surface value) and Downes et al. (2015) for the Southern Hemisphere (September; density changes by 0.03 kg m^{-3}).

5. Depth-integrated regimes

a. *Upper ocean above 700 m*

The upper ocean has an important role in exchanging heat and freshwater with the overlying atmosphere. Air–sea fluxes directly affect the ocean surface boundary layer (hereafter referred to as the mixed layer), which varies in depth depending on location and season (Fig. 3). In this section, we investigate how the surface heat and salt fluxes affect oceanic processes, particularly to understand the relationship between mixed layer processes and the upper-ocean regime of the SRT.

The air–sea heat and freshwater fluxes were computed with respect to the JRA55-do surface forcing and the ocean mean state over the last 20 out of 1000 years (Figs. 4a,b and 5a,b). The net air–sea heat flux is a result of radiative (shortwave and longwave) and turbulent (sensible and latent) heat fluxes (Fig. 4b), with minor contribution from other processes (i.e., PME, RIV, FRZ). In general, the net air–sea heat flux (Fig. 4a) warms the equatorial ocean, low-latitude eastern boundary regions, and across the zonally nonuniform 40°–55°S band in the Southern Ocean (Tamsitt et al. 2016), whereas it cools the ocean at midlatitudes in western boundary currents (WBCs) and at high latitudes (poleward of 50°). Regions of maximum deep mixed layers (Fig. 3) at high latitudes of both hemispheres lose heat to the atmosphere (Fig. 4a). The net surface freshwater fluxes have contributions from PME, RIV, RES, and ICE (Fig. 5b; restoring and sea ice salt fluxes were converted to equivalent freshwater fluxes for comparison). PME dominates the global patterns and RIV is of local importance only (Fig. 5a). RES plays a role in WBCs, the Antarctic Circumpolar Current (ACC), and high-latitude regions (not shown). ICE is the dominant contribution at high latitudes. Its effect is summarized by positive freshwater flux at the marginal sea ice zone (where sea ice melts) and negative freshwater fluxes at higher latitudes (where sea ice forms), resulting in a net equatorward freshwater flux in both hemispheres (Fig. 5b), similar to what has been recently shown for the Southern Ocean (Abernathey et al. 2016; Pellichero et al. 2018).

The zonally integrated budget for 0–700 m (Figs. 4d and 5d) reflects the dominant processes observed in Fig. 2; however, it shows that the significant downward transport by mean advection and upward transport by the eddy-induced transport vary across latitude, including changes in sign. The superposition of ADV and EIT—the super-residual transport—has similar magnitude and opposite contribution to the net surface heat and salt fluxes (see Figs. 4a,c and 5a,c). Although the other processes seem unimportant, a depth integration from 0 m rather than 10 m obscures the relevance of parameterized mixed layer processes, such as KPP and convection, that effectively redistribute the air–sea fluxes across the water column (Fig. 6).

To investigate the vertical redistribution by mixed layer processes, we divided the heat and salt convergences for the surface layer (0–10 m) and for a depth integration from 10 to 700 m (Fig. 6). Downward fluxes are represented by cooling/freshening at the surface and warming/salinification at subsurface (10–700 m), where the opposite holds for upward fluxes. In the heat budget, DIA and SWP are responsible for downward fluxes while KPP, CON, and SUB transport heat upward. In the salt budget, DIA transports salt upward and KPP, CON, and SUB transport salt downward. Processes such as KPP (heat),

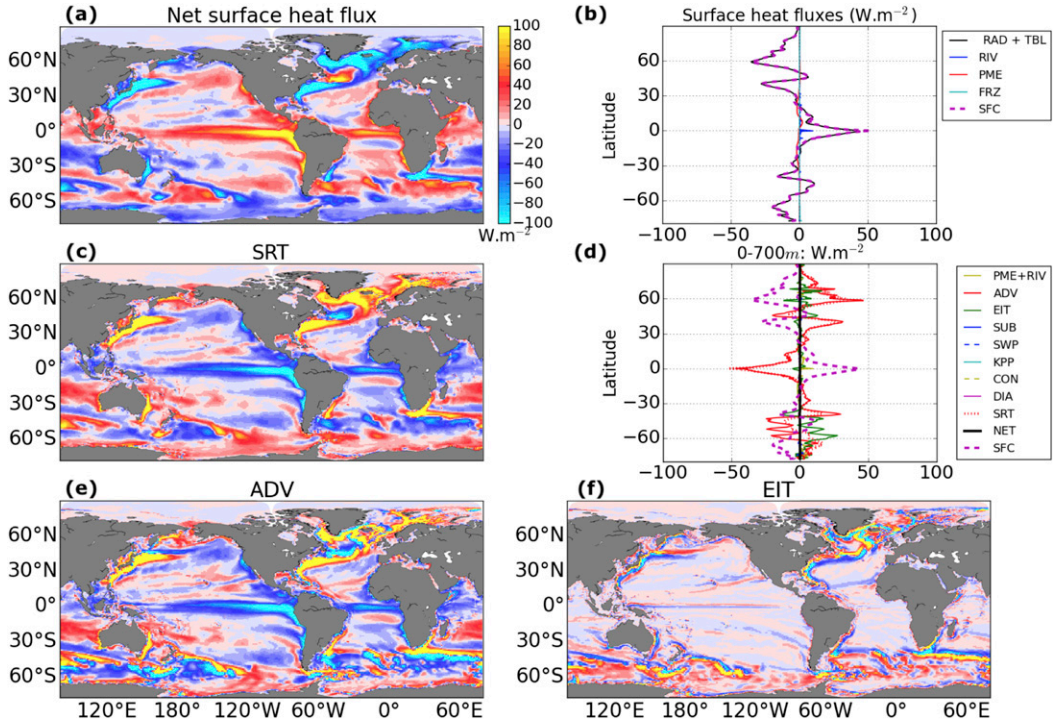

FIG. 4. Mean state of (a) net surface heat flux and (b) zonally integrated surface heat flux components (both in W m^{-2}) where positive (negative) values denote heat gain (loss) by the ocean. Depth-integrated (surface to 700 m) heat fluxes for the main processes: (c) superresidual transport, (e) mean advection, and (f) eddy-induced transport (W m^{-2}). (d) Zonally and depth-integrated (surface to 700 m) ocean heat transport components (W m^{-2}).

convection (heat and salt), and dianeutral diffusion (salt) respond to negative surface buoyancy forcing, and their effects reach far down in regions of deep mixed layers and are locally balanced by the SRT transport, as will be explained in section 6.

b. *Ocean interior below 700 m*

The zonally integrated heat and salt budgets of the dominant processes in the ocean interior (depth integrated from 700 m to the bottom) are shown in Figs. 7b and 8b. Downward heat/salt transport by ADV and upward transport by EIT are the main processes in the ocean interior. This balance mostly occurs in the midlatitudes (35°–60°) of both hemispheres and is dominated by the Southern Ocean, as found in previous studies (Gregory 2000; Kuhlbrodt et al. 2015). In our heat balance among ADV and EIT, from 700 m to the bottom (Table 3), the Southern Ocean explains 62% and 63% of the global (values correspond to contribution from ADV and EIT, respectively), the northern latitudes (north of 30°N) explains 27% and 30%, and the remaining 11% and 7% is found between 30°S and 30°N.

The major geographic patterns for the ADV and EIT are found along frontal regions associated with WBCs, the North Atlantic Current (NAC) and the ACC (Figs. 7e,f and 8e,f). In these frontal regions, there are dipoles of positive–negative fluxes, however, downward fluxes tend to dominate for ADV. Although we cannot separate between the various advective components, the dipole pattern in ADV, at least across the ACC front, is likely related to both the geostrophic (isopycnal slopes) component and the wind-driven component, which can steepen slopes if the wind blows downstream (e.g., westerly winds and the ACC), causing the lighter (heavier) side of the front to experience downward (upward) transport. In general, EIT acts against ADV, with a similar spatial distribution but opposite sign. In addition to frontal regions, ADV and EIT tend to be locally intensified above major topographic features such as the Drake Passage, the Kerguelen Plateau, and the Pacific–Antarctic Ridge, as well as in highly energetic regions such as the Brazil–Malvinas Confluence and the Agulhas Return Current (Tamsitt et al. 2018).

6. Connection between upper and interior regimes

The zonally integrated vertical distribution of the ADV and EIT is summarized in Figs. 9e,f and 10e,f). Although the ADV downward heat fluxes and the EIT upward heat fluxes are observed from mid- to high latitudes in both hemispheres, they extend deeper in the Southern Ocean

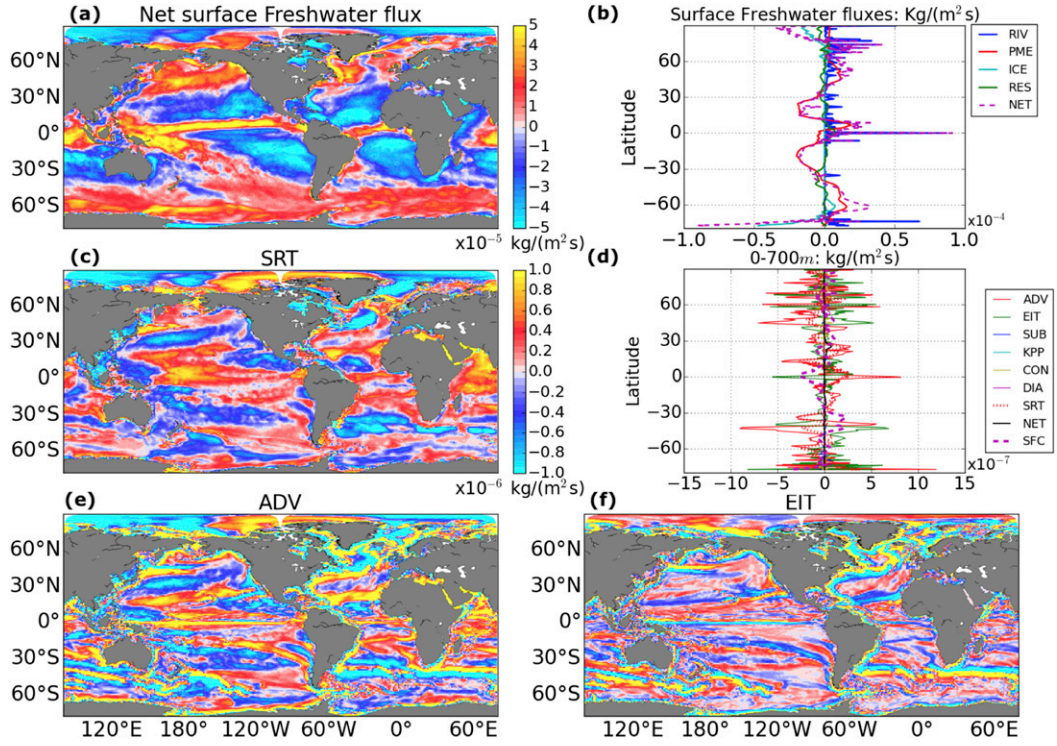

FIG. 5. Mean state of (a) net surface freshwater flux and (b) zonally integrated surface freshwater flux components (both in kg m^{-2} s^{-1} of freshwater), where positive (negative) values denote freshwater gain (loss) by the ocean. Depth-integrated (surface to 700 m) salt fluxes for the main processes: (c) superresidual transport, (e) mean advection, and (f) eddy-induced transport (kg m^{-2} s^{-1} of salt). (d) Zonally and depth-integrated (surface to 700 m) ocean salt transport components (kg m^{-2} s^{-1} of salt).

(from 200 to 4000 m) compared to Northern Hemisphere basins (from 200 to 2000 m). These fluxes traverse several water mass definitions (green contours, Table 4), with a peculiarity in the salt budget, where both ADV and EIT reverse sign around 1000–2000 m. This peculiarity is related to the southward and upward transport of relatively salty deep waters into the Southern Ocean, which is then modified by interior mixing with upper (AAIW) and lower (AABW) layers, to form Circumpolar Deep Water (CDW). Another peculiarity is a meridionally coherent feature seen in EIT and DIA poleward of 30° around 200 m in both hemispheres (and all ocean basins), which does not seem realistic. We speculate it to be related to the tapering scheme (Danabasoglu and McWilliams 1995) and/or due to a significant change in vertical resolution around 200 m in ACCESS (Bi et al. 2013).

The downward fluxes by ADV have been linked with the wind-driven vertical circulation (Gregory 2000; Wolfe et al. 2008), arising from the dominance of downwelling of warm water due to Ekman pumping over the upwelling of cold water due to Ekman suction. In addition, lateral variations in vertical transport can steepen the isopycnal slopes and increase baroclinicity, raising the available potential energy and the mesoscale activity. The release of potential energy by transient mesoscale eddies (eddy advection) acts to flatten the isopycnals in opposition to the mean flow, producing a time-mean upward heat transport that compensates (at least partially) the mean advective transport (Wolfe et al. 2008; Morrison et al. 2013; Zika et al. 2013; Griffies et al. 2015), largely confined along the paths of the strongest currents (WBCs, ACC, NAC; not shown). Upward fluxes also occur due to the isoneutral (eddy) diffusion where the isopycnals and isotherms are sloping (mostly in regions poleward of 35° in both hemispheres; see green and black contours in Fig. 9). The isoneutral diffusion also contributes to the same regions as the eddy advection, but it has a weaker and more widespread effect throughout mid- and high latitudes (not shown).

Even though ADV and EIT drive the largest heat and salt transports in the ocean interior, the globally integrated budgets show that it is the residual of these terms, the SRT, that is most useful for elucidating the regions and magnitudes of water mass formation and exchange. While ADV and EIT extend to deep layers across various water masses, poleward of 35°, the SRT contribution is largely confined to the upper 700 m (Figs. 9c and 10c). The SRT net effect is downward transport of heat and salt

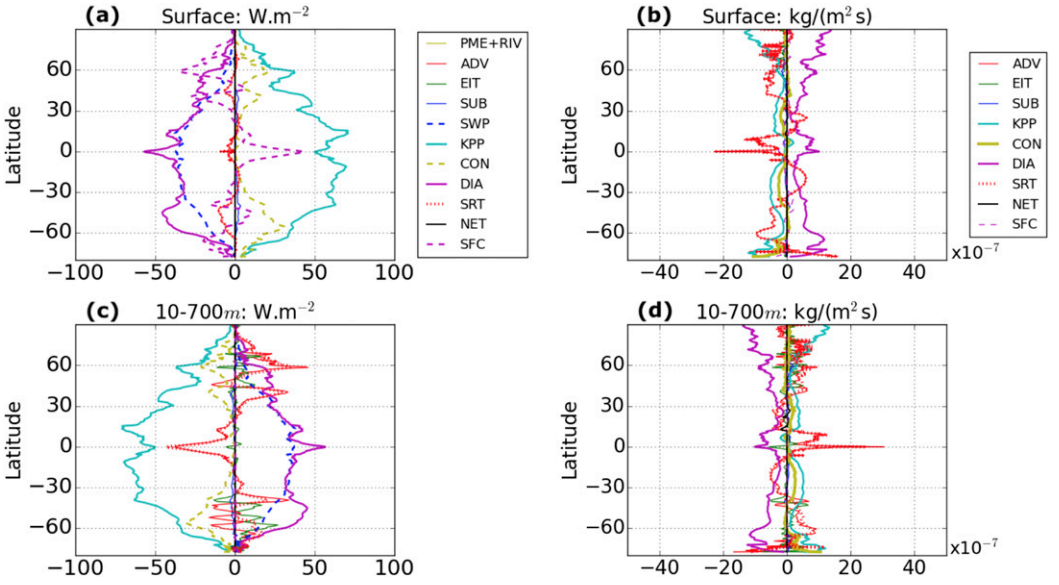

FIG. 6. Zonally integrated ocean (left) heat and (right) salt budgets at the (a),(b) ocean surface and (c),(d) depth integrated from 10 to 700 m. Units are W m^{-2} for the heat budget and kg m^{-2} s^{-1} for the salt budget. Positive (negative) is downward (upward) flux for both heat and salt.

to counterbalance upward transport from mixed layer processes (KPP, SUB, and CON for heat and salt, and DIA for salt) operating within mode waters (including SAMW in the Southern Ocean and in the Northern Hemisphere), intermediate waters and bottom waters in the Southern Ocean (AAIW and AABW), and deep waters in the Subpolar North Atlantic (NADW). These density ranges follow definitions in Iudicone et al. (2016), except for the AABW definition, which was based on Downes et al. (2015).

In the heat budget (Fig. 9), KPP and CON cool the subsurface ocean in regions of deep mixed layers, increasing the density of the subsurface upper ocean in response to the negative surface heat flux (as shown in section 5a). DIA also contributes to downward heat transport but has only secondary importance. In the salt budget (Fig. 10), DIA transports salt upward, but only at high latitudes (poleward of 50°) where the sea ice salt flux contributes. The SRT (and secondarily DIA for the heat budget) has a key role in balancing these mixed layer processes, transporting heat and salt downward. The downward transport of cold water from the mixed layer into the ocean interior can be seen as the removal of newly formed dense waters from their region of formation.

Away from the dense water formation sites (generally below 700 m), the dominant processes in the ocean interior reflect the global balance between SRT and DIA (Fig. 2). After removing the recently formed water masses from the mixed layer (section 5b), the SRT redistributes them along isopycnals into the ocean interior. The counterbalancing effect from DIA is interpreted as the small-scale mixing necessary to maintain the overturning circulation (Kuhlbrodt et al. 2007). This SRT–DIA balance is not uniformly distributed over depth (Figs. 9a,c and 10a,c) and geographically (Figs. 7a,c and 8a,c). The SRT–DIA balance shows maximum vertical heat transport at around 1500 and 3500 m (Fig. 2a). In Figs. 9a and 9c, this balance is largely identified below 1000 m and within 60°S–60°N, where the SRT effect is dominated by ADV at low latitudes, with EIT contribution mostly restricted to poleward of 35° (Figs. 9e,f). Our findings agree with recent theories that proposed that the conversion of dense to lighter water (downward heat transport) by dianeutral mixing occurs in a thin bottom layer (Ferrari et al. 2016; McDougall and Ferrari 2017) rather than in the ocean interior (Stommel and Arons 1960; Munk 1966). DIA is affected by the vertical diffusivity profile. Examination of zonal sections of vertical diffusivity that pass through regions of rough bottom topography support this assertion (not shown). Enhanced diffusivity near the bottom in ACCESS-OM2 only accounts for the parameterized breaking of internal waves over rough topography (not shown), as implemented in the tidal mixing scheme (Simmons et al. 2004).

To illustrate the regional patterns of heat and salt transport between the upper ocean and the ocean interior, we show the vertically integrated budgets between 300 and 1200 m (Figs. 11 and 12). This depth interval highlights processes occurring away from the largest fluxes near the surface (mostly above 200 m) but comprises a large portion

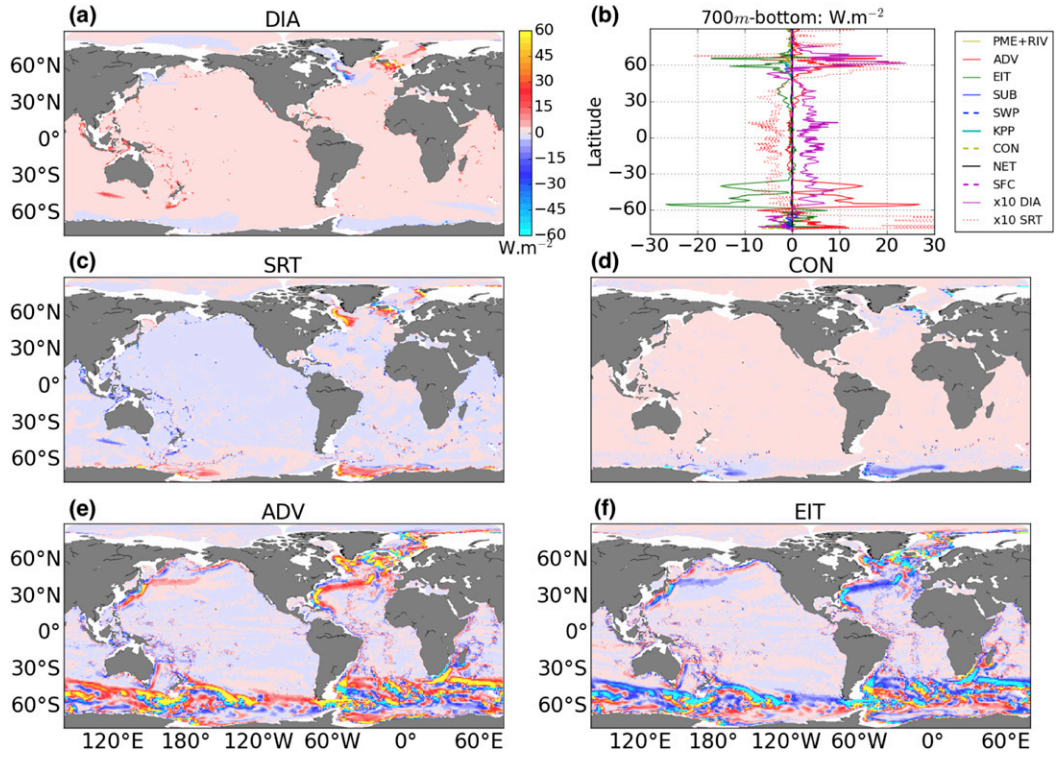

FIG. 7. Mean state of the depth integrated (700 m to bottom) ocean heat (W m^{-2}) for the main processes: (a) dianeutral diffusion, (c) superresidual transport, (d) convection, (e) mean advection, and (f) eddy-induced transport. (b) Zonally and depth integrated (700 m to bottom) for all ocean heat transport components (W m^{-2}). (b) The SRT–DIA balance magnified by a factor of 10 for clarity.

of deep mixed layers where dense water masses are formed and then transported to the ocean interior. The main SRT distribution at this depth range is clearly associated with deep mixed layers (Fig. 3). In the heat budget (Fig. 11), the SRT transports heat downward (with a secondary contribution from DIA), counterbalancing upward fluxes from KPP, SUB, and CON. In the salt budget (Fig. 12), DIA also contributes to upward salt transport. These upward heat and salt fluxes occur in the deep mixed layer regions where the air–sea heat fluxes have a strong cooling effect on the ocean surface (Fig. 4a). The vertical mixing by KPP and CON is a response to the negative buoyancy fluxes, leading to mixing of tracers and deepening of the mixed layer. Upward salt flux from DIA is associated with downward diffusion of freshwater. SUB acts only in the mixed layer with a restratification effect, resulting in upward heat and salt fluxes in the subsurface mixed layer.

7. Discussion

We presented ocean heat and salt budget analyses for a quasi-steady-state simulation from ACCESS-OM2. The dominant processes of vertical heat and salt transport were decomposed into regional processes for both the upper ocean and ocean interior. The superposition of the two main processes of vertical heat and salt transport, the mean advection and the eddy-induced transport, defined as the superresidual transport, reveals two opposite contributions over depth: the upper-ocean regime is largely associated with deep winter mixed layers where dense waters originate, while the ocean interior regime is associated with the recirculation of these dense waters. The latter regime can be seen as a reinterpretation of the classical advective–diffusive balance, although with important differences from the original theory with respect to the nonuniform distribution (Stommel and Arons 1960; Munk 1966).

Compared to past findings, our results are in agreement with recent studies that performed budget calculations for the upper 200 m. Hieronymus and Nycander (2013) highlighted the importance of the shortwave penetration and convection for the heat balance and of dianeutral diffusion, mean advection, and convection for the salt budget in the NEMO ocean–sea ice model. Similarly, Griffies et al. (2015) showed that KPP, shortwave penetration, and dianeutral diffusion are the main terms of the upper-200-m heat budget in a suite of GFDL coupled

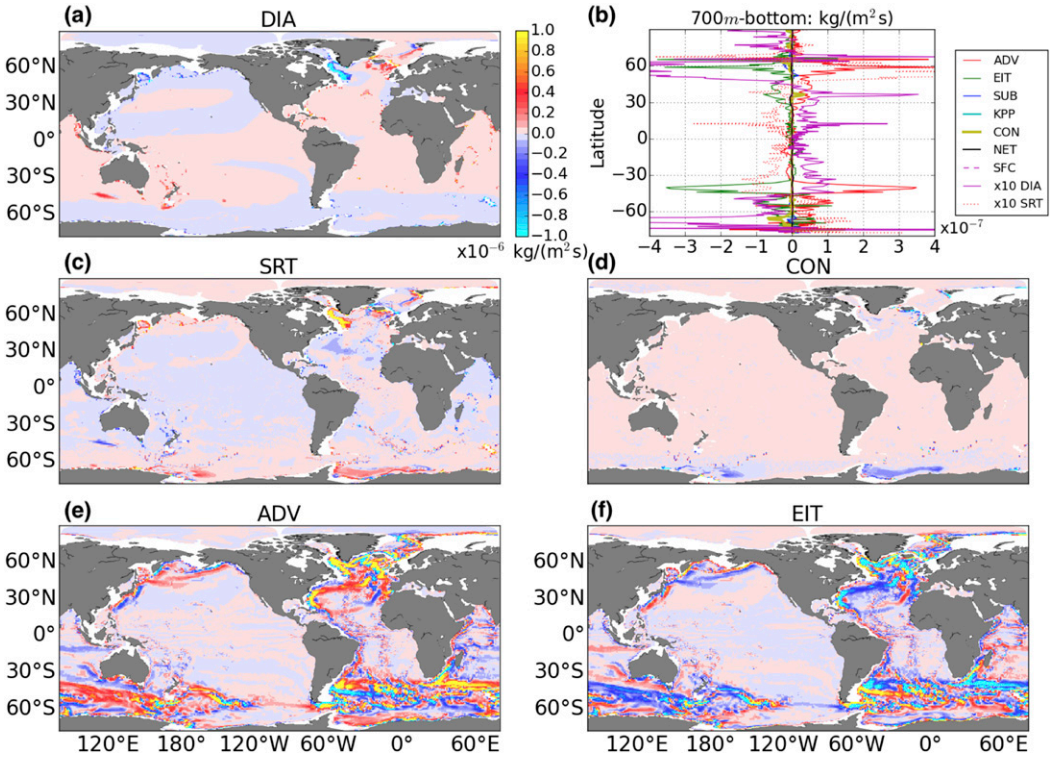

FIG. 8. Mean state of the depth integrated (700 m to bottom) ocean salt ($kg\,m^{-2}\,s^{-1}$) for the main processes: (a) dianeutral diffusion, (c) superresidual transport, (d) convection, (e) mean advection, and (f) eddy-induced transport. (b) Zonally and depth integrated (700 m to bottom) for all ocean salt transport components ($kg\,m^{-2}\,s^{-1}$). (b) The SRT–DIA balance magnified by a factor of 10 for clarity.

climate models (CM2.0, although they did not separate the convection term from dianeutral diffusion). Below 200 m, previous heat/salt budget studies showed that mean advection and eddy-induced transport dominate the vertical transport (e.g., Gregory 2000; Gnanadesikan et al. 2005; Wolfe et al. 2008; Hieronymus and Nycander 2013; Exarchou et al. 2015; Griffies et al. 2015). The total eddy transport has quantitatively similar contributions from both parameterized eddy advection GM90 and eddy (isoneutral) diffusion G98. Our results from ACCESS-OM2 show a similar role for those processes in the vertical transport, with a major contribution from the Southern Ocean (60% of the global), as noted in Gregory (2000) and Kuhlbrodt et al. (2015). However, by presenting a new interpretation of this vertical balance through the superresidual transport, we highlight its key role in the transport of newly formed dense water masses into the ocean interior, not detailed in previous studies.

In our study, the superresidual transport shows two distinct roles depending on depth, which we divided into upper-ocean and ocean-interior regimes. In the upper-ocean regime, within the winter deep mixed layer regions from both hemispheres (above 700 m in the global integral; Fig. 2), the SRT moves heat and salt downward. This transport compensates upward fluxes from nonlocal vertical mixing from KPP, submesoscale eddies, convection (heat and salt), and dianeutral diffusion (salt). The effect of dianeutral diffusion differs: downward (reinforcing SRT) for heat and upward (against SRT) for salt. The winter deep mixed layers are triggered by strong negative surface buoyancy fluxes but vary in depth depending on location (not shown). Convection and KPP actively respond to the negative surface fluxes over the whole mixed layer column (Fig. 3).

TABLE 3. Contribution of the main processes (%) to positive/negative heat fluxes per regions: southern latitudes (south of 30°S), low latitudes (30°S–30°N), and northern latitudes (north of 30°N). The values are depth integrated (700 m to bottom) zonally and meridionally between the given latitudinal bounds. We only integrated the grid points where the DIA and ADV have positive (downward) transport and the EIT and CON have negative (upward) transport.

Process	Transport	Southern latitudes	Low latitudes	Northern latitudes
ADV	⇓	62	11	27
EIT	⇓	63	7	30
DIA	⇓	24	32	44
CON	⇑	70	1	29

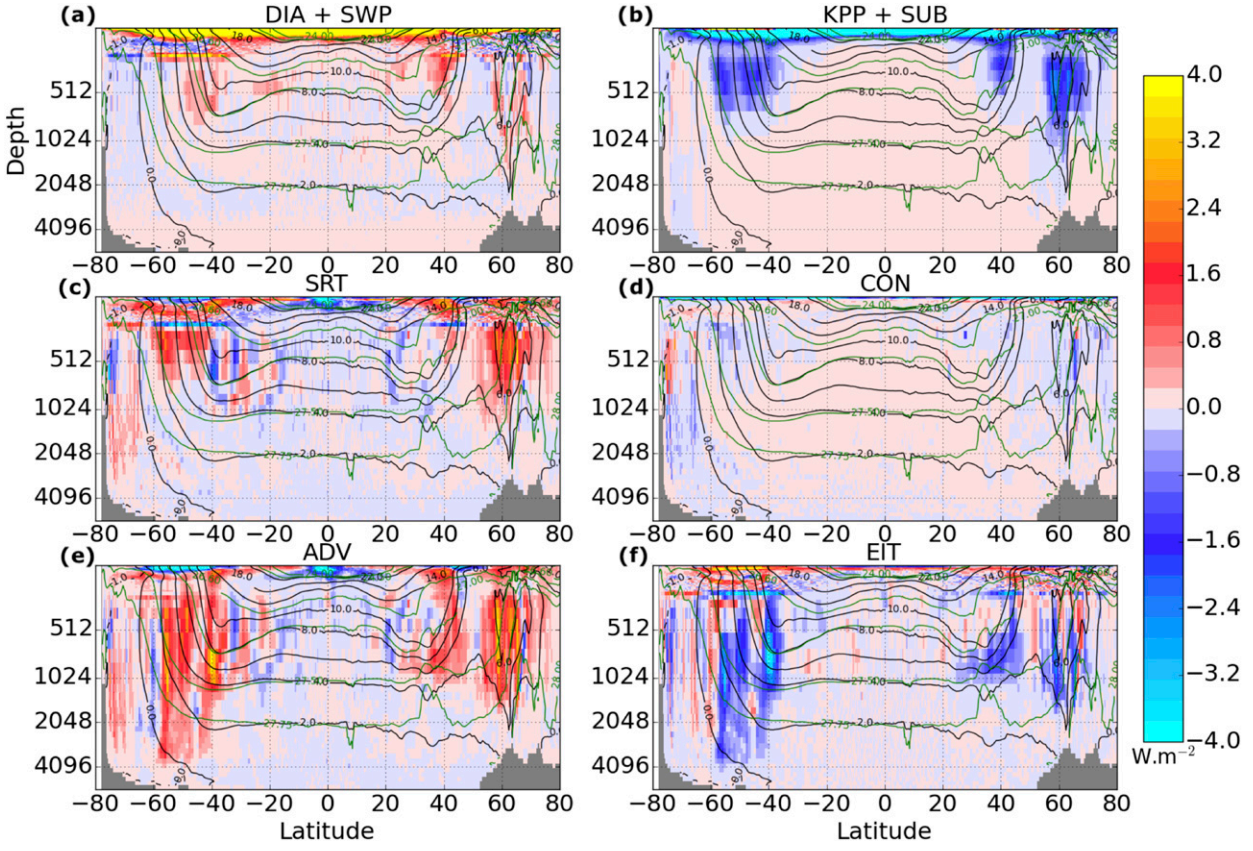

FIG. 9. Mean state of the zonally integrated ocean heat budget (W m^{-2}) for the following processes: (a) dianeutral diffusion plus shortwave penetration, (b) nonlocal KPP plus submesoscale eddies, (c) superresidual transport, (d) convection and overflow, (e) mean advection, and (f) eddy-induced transport. The depth axes are plotted in $\log_2$ for a clear view of the upper-ocean processes. Black isotherms have an interval of 2°C. Green isopycnals show water masses as defined in Table 4.

In the band between 40° and 60°S, winter deep mixed layers, where dense water masses are formed (e.g., Marshall et al. 1993), are especially found on the eastern Indian and Pacific Ocean sectors, where the ACC shifts poleward and where a zonal asymmetry in air–sea flux products is observed (Cerovečki et al. 2011; Tamsitt et al. 2016). In these areas, upward heat fluxes reach 700 m, associated with mode and intermediate waters (SAMW and AAIW), and transform relatively warm and salty deep waters into lighter (colder and fresher) waters (Figs. 9b,d). Lagrangian trajectories from an ocean state estimation confirm that this water mass transformation occurs below surface layers (Tamsitt et al. 2018). However, the effect of vertical redistribution processes (KPP and convection) was deemed secondary in observational and reanalysis-based mixed layer heat budgets (Dong et al. 2007; Tamsitt et al. 2016). Our analyses indicate that these two processes actually play an essential role in the formation of dense waters (SAMW, AAIW, NADW, AABW).

In terms of AAIW formation due to freshwater fluxes, we find that equatorward transport is dominated by the ICE fluxes (Fig. 5b), resulting from positive surface salt fluxes due to sea ice formation near the coast and negative salt fluxes near the marginal zones where sea ice melts and AAIW originates (Pellichero et al. 2018). These fluxes are maximum during late winter and spring when sea ice melting is larger (not shown) and can be linked with the first stage of AAIW transformation as described in Evans et al. (2018). In ACCESS-OM2, however, large salinity restoring fluxes occur due to biases associated with a weaker and less penetrative AAIW salinity minimum tongue relative to observations (see region between 30° and 45°S in Fig. 5b), a common bias in ocean models (Bi et al. 2013; Downes et al. 2015). The AAIW positive temperature and salinity biases [see Figs. 12a and 12b of Kiss et al. (2019)] combined with an overestimation of the SAMW low potential vorticity (Downes et al. 2015) results in the warming drift centered at 700 m (Fig. 1).

High latitudes of the North Atlantic, where winter deep mixed layers are observed (e.g., Talley and McCartney 1982; Swift 1984; Dickson and Brown 1994), are important formation regions for NADW. We find strong upward

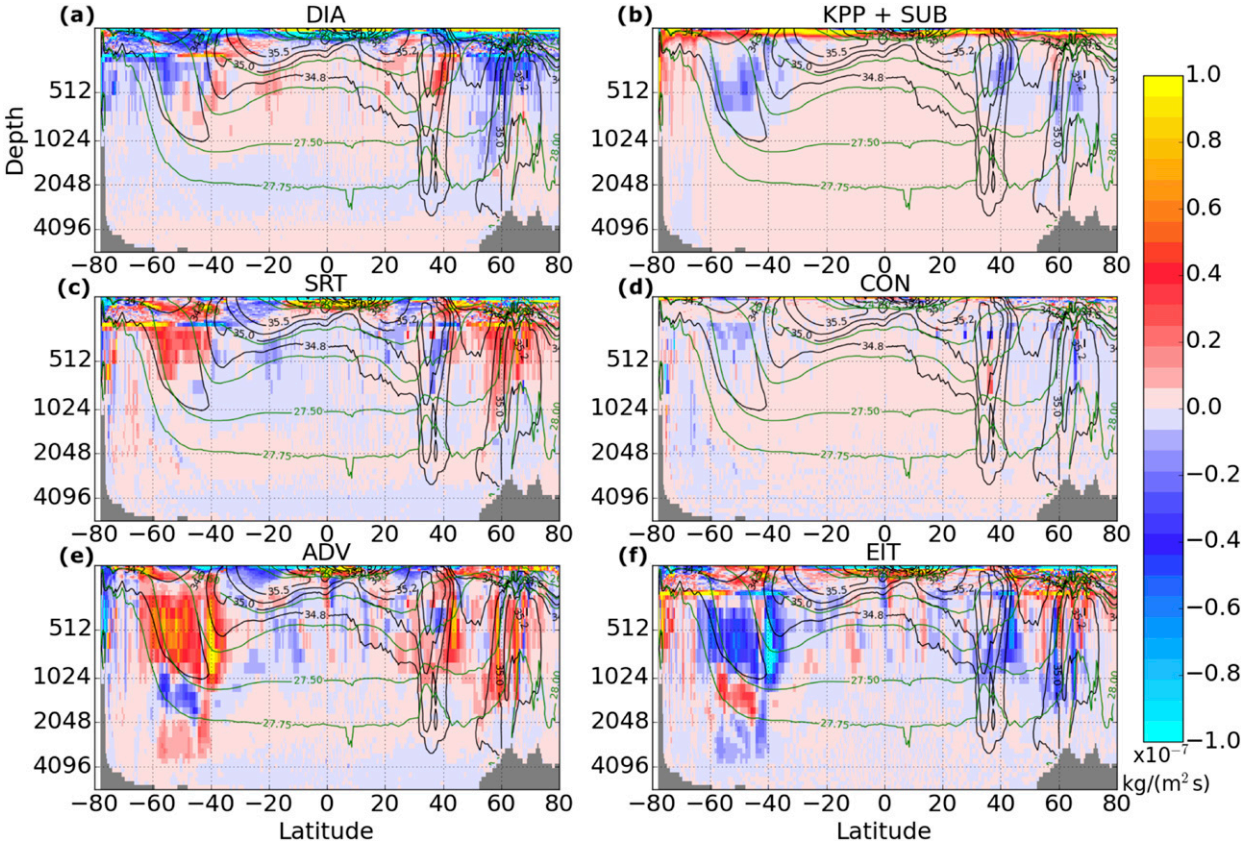

FIG. 10. As in Fig. 9, but for ocean salt budget ($kg\,m^{-2}\,s^{-1}$). Black isohalines have an interval of 0.5 psu. Green isopycnals show water masses as defined in Table 4.

heat fluxes within deep mixed layers in the Labrador Sea, south of Iceland, and southeast of Svalbard (Figs. 11a,b,d and 12a,b,d). While in the Labrador Sea and south of Greenland, these upward fluxes [and the mixed layer depth (MLD)] reach depths greater than 2000 m, in the Greenland–Iceland–Norwegian Seas, upward heat fluxes are shallower (around 1500 m), consistent with the mid-depth convection expected for these regions (Aagaard and Carmack 1989). There is a large variety of subgridscale processes in high latitudes that play a role in ventilating the deep ocean (Palter et al. 2014). In particular, we note that the connection of the surface buoyancy fluxes with water parcels in the deep mixed layers is done by convection and KPP in the heat budget and dianeutral diffusion in the salt budget. Although significant model temperature, salinity and MLD biases are generally seen in the North Atlantic Subpolar Gyre (Danabasoglu et al. 2014), the ACCESS-OM2 has good representation of the AMOC transport strength, with a seasonal average of 16 Sv ($1\,Sv \equiv 10^6\,m^3\,s^{-1}$) (not shown) that agrees well with observations from the RAPID mooring array at 26.5°N (McCarthy et al. 2015).

The deep mixed layer regions around the Antarctic continent also contribute to dense water mass formation. For AABW formation, these MLDs are found in the Weddell and Ross Seas, where convection to the seafloor dominates the upward heat transport south of 60°S (see Figs. 7b,d). The formation of large polynyas in those seas is common in ocean models (de Lavergne et al. 2014), allowing unrealistic open-ocean convection to occur, which can produce excessive AABW, usually associated with a cooling model drift in the ocean abyss (Griffies et al. 2009; Bi et al. 2013). Although this is not a desirable feature in climate simulations, previous occurrences of the Weddell polynya have been recorded in the 1970s

TABLE 4. Water mass definitions in σ_Θ, based on Iudicone et al. (2016).

Water mass	Density interval (σ_Θ)
Tropical water	<24.5
Subtropical mode water	24.5–26.6
Subpolar mode water	26.6–27.0
Intermediate water	27.0–27.5
Deep water	27.5–27.75
Bottom water	>27.75

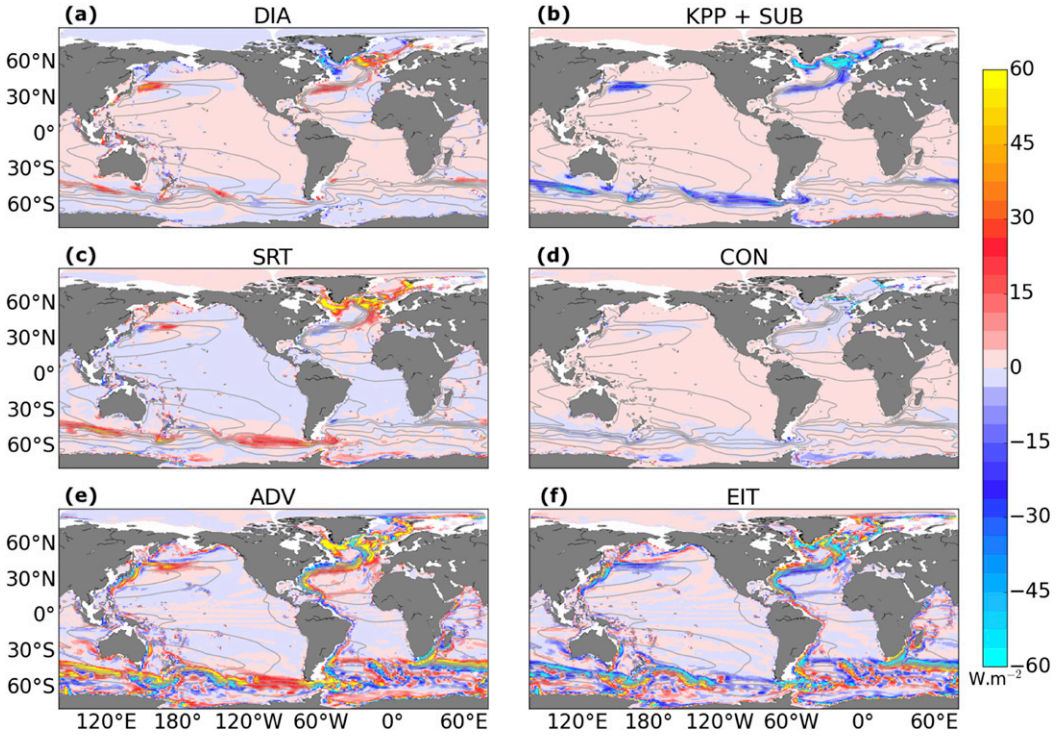

FIG. 11. Depth-integrated (300–1200 m) ocean heat budget (W m^{-2}): (a) dianeutral diffusion, (b) nonlocal KPP plus submesoscale eddies, (c) superresidual transport, (d) convection and overflow, (e) mean advection, and (f) eddy-induced transport. Gray isothermals have an interval of 1.25°C.

(Zwally and Gloersen 1977; Carsey 1980; Gordon and Comiso 1988) and in recent years (Campbell et al. 2019). In addition to convection within the polynyas, our results show strong vertical fluxes over the continental shelf (see Figs. 11b,d), not only in the Weddell and Ross Seas but also in spots along the East Antarctic sector. Although the PME dominates the surface freshwater fluxes at most regions, the ICE and RIV fluxes are the main contributors poleward of 70° (both hemispheres; Fig. 5b). The negative freshwater fluxes due to brine rejection during wintertime helps to destabilize the water column and strengthen convection.

For the ocean-interior regime, the superresidual transport has an opposite contribution to that in regions of deep mixed layers. As the superresidual transport removes recently formed dense waters from mixed layers (warming), it has a cooling effect below the deep mixed layers as these water masses are transported along their respective neutral surfaces. This upward heat transport (cooling effect) in the ocean interior is counterbalanced by downward transport through dianeutral diffusion. We interpreted this as transport of cold waters in the ocean interior along with turbulent mixing with adjacent water masses. While previous studies found that the advective cooling of AABW is compensated by dianeutral diffusion below 3000 m (Kuhlbrodt et al. 2015; Exarchou et al. 2015; Griffies et al. 2015), our findings associate the SRT with the transport of all main dense waters that fill the ocean interior (mode, intermediate, deep, and bottom waters) largely below 700 m, as indicated by the sign change of SRT from positive to negative at 700 m in Fig. 2, and seen in the balance between DIA and SRT in the global integrals of Figs. 9a and 9c. This is a key component of our interpretation of the budget using the superresidual approach.

While analyzing the tracer budget under the superresidual perspective does not disregard the fact that the mean advection and eddy-induced transport are the largest contributions for global vertical transport, this approach reveals a novel insight of the role of the advective–diffusive balance for budget analyses. Prior studies emphasized that the advective–diffusive balance suggested by Munk (1966) is largely negligible to the global heat budget (Palter et al. 2014; Kuhlbrodt et al. 2015). However, reinterpreting the effective water mass redistribution by SRT as the "advective" component, an advective–diffusive balance in the ocean interior seems remarkably appropriate.

Aligned with in situ observations (Polzin 1997; St. Laurent et al. 2001, 2012) and recent theories for the abyssal circulation (Ferrari et al. 2016; McDougall and

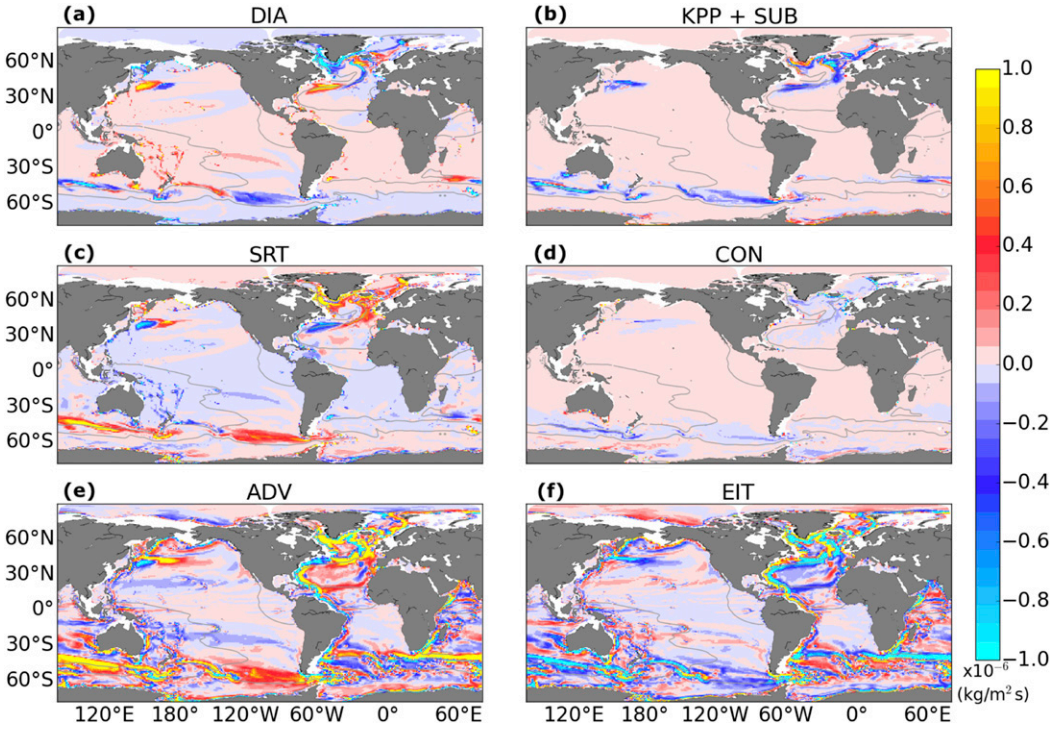

FIG. 12. As in Fig. 11, but for ocean salt budget ($kg\,m^{-2}\,s^{-1}$). Gray isohalines have an interval of 0.5 psu.

Ferrari 2017), we find that the vertical distribution of the dianeutral mixing is not globally uniform. The strongest mixing of bottom waters in ACCESS-OM2 occurs mostly in regions of rough topography, in support of recent findings (Ferrari et al. 2016; Holmes et al. 2018), where internal tides dissipate energy (Simmons et al. 2004; Melet et al. 2016) and shape the abyssal circulation (de Lavergne et al. 2017). One caveat is that our model simulation does not include geothermal heating (and other sources of internal mixing). Geothermal heating is expected to affect the near-bottom ocean temperature and overturning circulation (Emile-Geay and Madec 2009; Mashayek et al. 2013; Downes et al. 2016; de Lavergne et al. 2016) and therefore to play a potentially large role in the deep ocean heat budget (Hieronymus and Nycander 2013). By driving upward heat transport near the bottom, it is expected to reinforce the abyssal circulation (Ferrari et al. 2016).

8. Conclusions

To summarize, after spinning up the ACCESS-OM2 model under JRA55-do repeat year forcing, we found the global heat and salt budgets are quantitatively dominated by the downward fluxes from the large-scale advection and upward fluxes from mesoscale eddy advection and diffusion (isopycnal) in most parts of the ocean interior. In agreement with previous studies, the Southern Ocean dominates this balance, representing between 62% and 63% of the overall global heat balance below 700 m, against 27%–30% for the northern oceans and 7%–11% from the tropical regions.

The residual of these dominant processes, defined here as the superresidual transport, has a key role in the formation and redistribution of water masses as a major driver of overall heat and salt transport (Fig. 13). Vertical mixing of heat, dianeutral diffusion of salt, convection, and submesoscale restratification drive upward fluxes as part of the formation of dense waters in regions of deep winter mixed layers. In an equilibrated state, these fluxes are compensated by downward fluxes primarily from the superresidual transport (with a secondary contribution via dianeutral diffusion of heat), which can be interpreted as removal of these dense waters from regions of formation into the adjacent ocean interior. Away from dense water formation regions, the superresidual transport acts to move these waters into their respective neutral layers, generally reflected in upward heat and salt fluxes balanced by dianeutral mixing. This superresidual transport and dianeutral diffusion balance is a contemporary interpretation of the classical advective–diffusive balance, where the advective part corresponds to the sum of large-scale and mesoscale eddy processes and the diffusive part is associated with the turbulent mixing across deep and

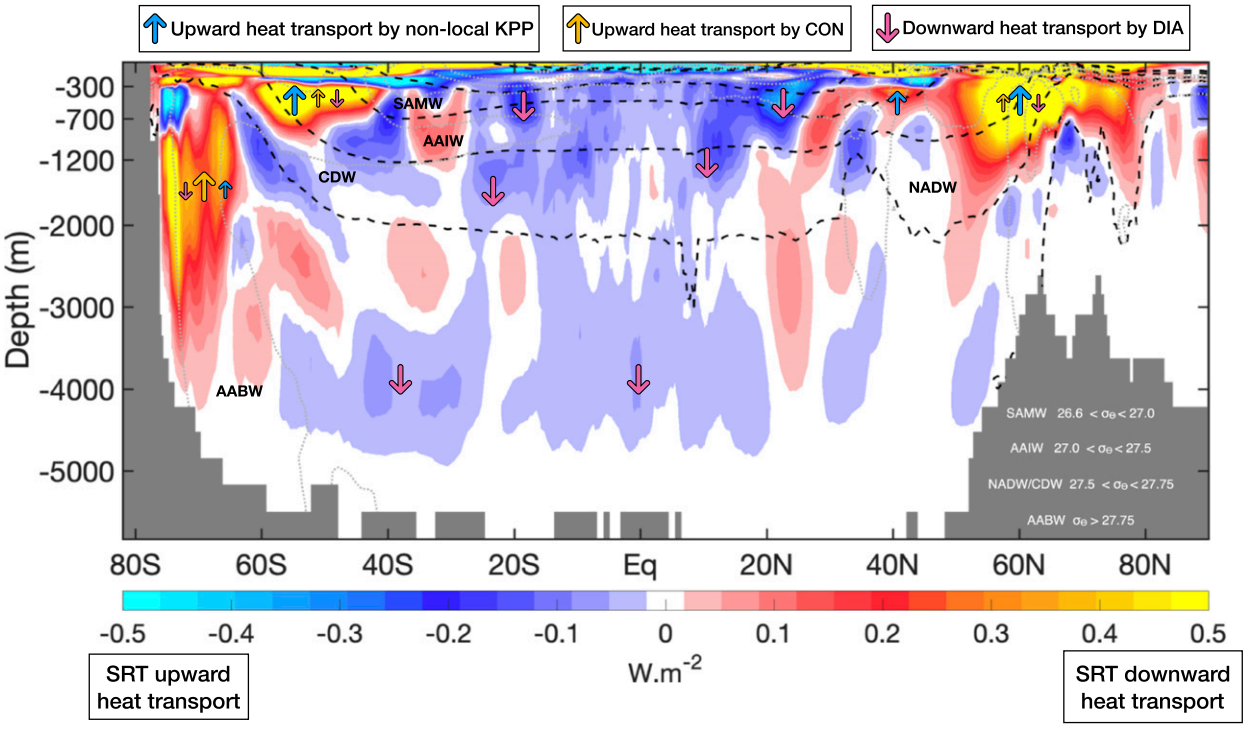

FIG. 13. Schematic of the superresidual framework. The colormap is the mean state of the zonally integrated superresidual transport (SRT = ADV + EIT), using a two-gridcell smoother, where positive values denote downward heat transport and negative values represent upward heat transport. Black dashed lines represent the isopycnals of water mass interfaces according to Table 4. Gray dashed lines represent the isohaline contours. The balance between convective (yellow arrows) and mixed layer (blue arrows) processes and the superresidual transport occurs in the deep mixed layers, identified in the schematic by the strong downward heat transport by SRT. The balance between dianeutral diffusion (red arrows) and the superresidual transport is found in the ocean interior at a range of depths and away from the mixed layers.

bottom waters. Our budget results support recent studies that found dianeutral mixing to have important spatial variability, being the abyssal mixing of bottom waters with lighter waters above, associated with internal waves breaking over rough topography (Polzin 1997; Ferrari et al. 2016).

The inspection of the superresidual transport in addition to the large-scale circulation and mesoscale eddy transport in budget analyses has important implications. First, the definition of SRT is useful for intermodel comparison with different grid resolutions; the isoneutral diffusion, for example, is intrinsically included in SRT either if it is parameterized (by eddy-induced transport) or not (accounted by resolved advection), as in eddy-permitting models (Kuhlbrodt et al. 2015). Second, the SRT can be used to calibrate simple climate models (e.g., MAGICC, Meinshausen et al. 2011) that rely on the vertical advective–diffusive balance, an essential tool for policy advice on mitigation strategies (Huber et al. 2015). Third, it elucidates a significant connection between the residual of the dominant processes of vertical transport and the processes that were previously thought of secondary importance; the mechanisms of water mass formation and erosion highlight the model dependence on subgridscale parameterizations, such as vertical mixing, convection, submesoscale eddies, and the vertical diffusion due to internal tides. Further intermodel comparison in the scope of FAFMIP (Gregory et al. 2016) and OMIP (Griffies et al. 2016) using the budget analysis and the superresidual approach can give important direct insights on how different ocean models represent physical processes and thus impact on uptake of tracers, ocean circulation, and sea level patterns.

Acknowledgments. This work is supported by the Australian Research Council Discovery Grant 160103130, ARC Centre of Excellence for Climate Extremes, and the National Computational Infrastructure through the National Computational Merit Allocation Scheme. FBD is supported by a Tasmanian Graduate Research Scholarship and CSIRO-UTAS Quantitative Marine Science top-up. CMD is supported by an ARC Future Fellowship FT130101532. SJM is supported through funding from the Earth Systems and Climate Change Hub of the Australian

Government's National Environmental Science Program. We are thankful for the support from the Consortium for Ocean–Sea Ice Modelling in Australia (COSIMA) and to Veronica Tamsitt and Louis A. H. R. Clement for useful comments on the manuscript. We thank the three anonymous reviewers for their comments that greatly helped to improve the clarity of the presentation.

REFERENCES

Aagaard, K., and E. C. Carmack, 1989: The role of sea ice and other fresh water in the Arctic circulation. *J. Geophys. Res.*, **94**, 14 485–14 498, https://doi.org/10.1029/JC094iC10p14485.

Abernathey, R. P., I. Cerovecki, P. R. Holland, E. Newsom, M. Mazloff, and L. D. Talley, 2016: Water-mass transformation by sea ice in the upper branch of the Southern Ocean overturning. *Nat. Geosci.*, **9**, 596–601, https://doi.org/10.1038/ngeo2749.

Adcroft, A., C. Hill, and J. Marshall, 1997: Representation of topography by shaved cells in a height coordinate ocean model. *Mon. Wea. Rev.*, **125**, 2293–2315, https://doi.org/10.1175/1520-0493(1997)125<2293:ROTBSC>2.0.CO;2.

Bi, D., and Coauthors, 2013: ACCESS-OM: The ocean and sea-ice core of the ACCESS coupled model. *Aust. Meteor. Oceanogr. J.*, **63**, 213–232, https://doi.org/10.22499/2.6301.014.

Boccaletti, G., R. Ferrari, and B. Fox-Kemper, 2007: Mixed layer instabilities and restratification. *J. Phys. Oceanogr.*, **37**, 2228–2250, https://doi.org/10.1175/JPO3101.1.

Bouttes, N., and J. M. Gregory, 2014: Attribution of the spatial pattern of CO_2-forced sea level change to ocean surface flux changes. *Environ. Res. Lett.*, **9**, 034004, https://doi.org/10.1088/1748-9326/9/3/034004.

Campbell, E. C., E. A. Wilson, K. Moore, S. C. Riser, C. E. Brayton, M. R. Mazloff, and L. D. Talley, 2019: Antarctic offshore polynyas linked to Southern Hemisphere climate anomalies. *Nature*, **570**, 319–325, https://doi.org/10.1038/s41586-019-1294-0.

Carsey, F. D., 1980: Microwave observation of the Weddell polynya. *Mon. Wea. Rev.*, **108**, 2032–2044, https://doi.org/10.1175/1520-0493(1980)108<2032:MOOTWP>2.0.CO;2.

Cerovečki, I., L. D. Talley, and M. R. Mazloff, 2011: A comparison of Southern Ocean air–sea buoyancy flux from an ocean state estimate with five other products. *J. Climate*, **24**, 6283–6306, https://doi.org/10.1175/2011JCLI3858.1.

Church, J. A., D. Monselesan, J. M. Gregory, and B. Marzeion, 2013: Evaluating the ability of process based models to project sea-level change. *Environ. Res. Lett.*, **8**, 014051, https://doi.org/10.1088/1748-9326/8/1/014051.

Danabasoglu, G., and J. C. McWilliams, 1995: Sensitivity of the global ocean circulation to parameterizations of mesoscale tracer transports. *J. Climate*, **8**, 2967–2987, https://doi.org/10.1175/1520-0442(1995)008<2967:SOTGOC>2.0.CO;2.

——, and Coauthors, 2014: North Atlantic simulations in Coordinated Ocean-ice Reference Experiments phase II (CORE-II). Part I: Mean states. *Ocean Modell.*, **73**, 76–107, https://doi.org/10.1016/j.ocemod.2013.10.005.

de Lavergne, C., J. B. Palter, E. D. Galbraith, R. Bernardello, and I. Marinov, 2014: Cessation of deep convection in the open Southern Ocean under anthropogenic climate change. *Nat. Climate Change*, **4**, 278–282, https://doi.org/10.1038/nclimate2132.

——, G. Madec, J. Le Sommer, A. J. G. Nurser, and A. C. Naveira Garabato, 2016: On the consumption of Antarctic Bottom Water in the abyssal ocean. *J. Phys. Oceanogr.*, **46**, 635–661, https://doi.org/10.1175/JPO-D-14-0201.1.

——, ——, F. Roquet, R. M. Holmes, and T. J. McDougall, 2017: Abyssal ocean overturning shaped by seafloor distribution. *Nature*, **551**, 181–186, https://doi.org/10.1038/nature24472.

Dickson, R. R., and J. Brown, 1994: The production of North Atlantic Deep Water: Sources, rates, and pathways. *J. Geophys. Res.*, **99**, 12 319–12 341, https://doi.org/10.1029/94JC00530.

Dong, S., S. T. Gille, and J. Sprintall, 2007: An assessment of the Southern Ocean mixed layer heat budget. *J. Climate*, **20**, 4425–4442, https://doi.org/10.1175/JCLI4259.1.

Downes, S. M., and Coauthors, 2015: An assessment of Southern Ocean water masses and sea ice during 1988–2007 in a suite of interannual CORE-II simulations. *Ocean Modell.*, **94**, 67–94, https://doi.org/10.1016/j.ocemod.2015.07.022.

——, A. M. Hogg, S. M. Griffies, and B. L. Samuels, 2016: The transient response of Southern Ocean circulation to geothermal heating in a global climate model. *J. Climate*, **29**, 5689–5708, https://doi.org/10.1175/JCLI-D-15-0458.1.

Emile-Geay, J., and G. Madec, 2009: Geothermal heating, diapycnal mixing and the abyssal circulation. *Ocean Sci.*, **5**, 203–217, https://doi.org/10.5194/os-5-203-2009.

Evans, D. G., J. D. Zika, A. C. Naveira Garabato, and A. J. G. Nurser, 2018: The cold transit of Southern Ocean upwelling. *Geophys. Res. Lett.*, **45**, 13 386–13 395, https://doi.org/10.1029/2018GL079986.

Exarchou, E., T. Kuhlbrodt, J. M. Gregory, and R. S. Smith, 2015: Ocean heat uptake processes: A model intercomparison. *J. Climate*, **28**, 887–908, https://doi.org/10.1175/JCLI-D-14-00235.1.

Eyring, V., S. Bony, G. A. Meehl, C. A. Senior, B. Stevens, R. J. Stouffer, and K. E. Taylor, 2016: Overview of the Coupled Model Intercomparison Project Phase 6 (CMIP6) experimental design and organization. *Geosci. Model Dev.*, **9**, 1937–1958, https://doi.org/10.5194/gmd-9-1937-2016.

Ferrari, R., and D. Ferreira, 2011: What processes drive the ocean heat transport? *Ocean Modell.*, **38**, 171–186, https://doi.org/10.1016/j.ocemod.2011.02.013.

——, S. Griffies, G. Nurser, and G. K. Vallis, 2010: A boundary-value problem for the parameterized mesoscale eddy transport. *Ocean Modell.*, **32**, 143–156, https://doi.org/10.1016/j.ocemod.2010.01.004.

——, A. Mashayek, T. J. McDougall, M. Nikurashin, and J.-M. Campin, 2016: Turning ocean mixing upside down. *J. Phys. Oceanogr.*, **46**, 2239–2261, https://doi.org/10.1175/JPO-D-15-0244.1.

Fox-Kemper, B., and Coauthors, 2011: Parameterization of mixed layer eddies. III: Implementation and impact in global ocean climate simulations. *Ocean Modell.*, **39**, 61–78, https://doi.org/10.1016/j.ocemod.2010.09.002.

Gent, P. R., and J. C. McWilliams, 1990: Isopycnal mixing in ocean circulation models. *J. Phys. Oceanogr.*, **20**, 150–155, https://doi.org/10.1175/1520-0485(1990)020<0150:IMIOCM>2.0.CO;2.

Gnanadesikan, A., R. D. Slater, P. S. Swathi, and G. K. Vallis, 2005: The energetics of ocean heat transport. *J. Climate*, **18**, 2604, https://doi.org/10.1175/JCLI3436.1.

Gordon, A. L., and J. C. Comiso, 1988: Polynyas in the Southern Ocean the global heat engine that couples the ocean and the atmosphere. *Sci. Amer.*, **258**, 90–97, https://doi.org/10.1038/scientificamerican0688-90.

Gregory, J. M., 2000: Vertical heat transports in the ocean and their effect on time-dependent climate change. *Climate Dyn.*, **16**, 501–515, https://doi.org/10.1007/s003820000059.

——, and Coauthors, 2016: The Flux-Anomaly-Forced Model Intercomparison Project (FAFMIP) contribution to CMIP6:

Investigation of sea-level and ocean climate change in response to CO2 forcing. *Geosci. Model Dev.*, **9**, 3993–4017, https://doi.org/10.5194/gmd-9-3993-2016.

Griffies, S. M., and R. W. Hallberg, 2000: Biharmonic friction with a Smagorinsky-like viscosity for use in large-scale eddy-permitting ocean models. *Mon. Wea. Rev.*, **128**, 2935–2946, https://doi.org/10.1175/1520-0493(2000)128<2935:BFWASL>2.0.CO;2.

——, and R. J. Greatbatch, 2012: Physical processes that impact the evolution of global mean sea level in ocean climate models. *Ocean Modell.*, **51**, 37–72, https://doi.org/10.1016/j.ocemod.2012.04.003.

——, A. Gnanadesikan, R. C. Pacanowski, V. D. Larichev, J. K. Dukowicz, and R. D. Smith, 1998: Isoneutral diffusion in a *z*-coordinate ocean model. *J. Phys. Oceanogr.*, **28**, 805–830, https://doi.org/10.1175/1520-0485(1998)028<0805:IDIAZC>2.0.CO;2.

——, and Coauthors, 2009: Coordinated Ocean-ice Reference Experiments (COREs). *Ocean Modell.*, **26**, 1–46, https://doi.org/10.1016/j.ocemod.2008.08.007.

——, and Coauthors, 2015: Impacts on ocean heat from transient mesoscale eddies in a hierarchy of climate models. *J. Climate*, **28**, 952–977, https://doi.org/10.1175/JCLI-D-14-00353.1.

——, and Coauthors, 2016: OMIP contribution to CMIP6: Experimental and diagnostic protocol for the physical component of the Ocean Model Intercomparison Project. *Geosci. Model Dev.*, **9**, 3231–3296, https://doi.org/10.5194/gmd-9-3231-2016.

Hieronymus, M., and J. Nycander, 2013: The budgets of heat and salinity in NEMO. *Ocean Modell.*, **67**, 28–38, https://doi.org/10.1016/j.ocemod.2013.03.006.

Holmes, R. M., C. de Lavergne, T. J. McDougall, R. M. Holmes, C. de Lavergne, and T. J. McDougall, 2018: Ridges, seamounts, troughs, and bowls: Topographic control of the dianeutral circulation in the abyssal ocean. *J. Phys. Oceanogr.*, **48**, 861–882, https://doi.org/10.1175/JPO-D-17-0141.1.

Huber, M., R. Tailleux, D. Ferreira, T. Kuhlbrodt, and J. Gregory, 2015: A traceable physical calibration of the vertical advection-diffusion equation for modeling ocean heat uptake. *Geophys. Res. Lett.*, **42**, 2333–2341, https://doi.org/10.1002/2015GL063383.

Hunke, E. C., W. H. Lipscomb, A. K. Turner, N. Jeffery, and S. Elliott, 2013: CICE: The Los Alamos Sea Ice Model Documentation and Software User's Manual LA-CC-06-012. Tech. Rep., 115 pp.

Iudicone, D., K. B. Rodgers, Y. Plancherel, O. Aumont, T. Ito, R. M. Key, G. Madec, and M. Ishii, 2016: The formation of the ocean's anthropogenic carbon reservoir. *Sci. Rep.*, **6**, 35473, https://doi.org/10.1038/srep35473.

Jochum, M., 2009: Impact of latitudinal variations in vertical diffusivity on climate simulations. *J. Geophys. Res.*, **114**, C01010, https://doi.org/10.1029/2008JC005030.

Kiss, A. E., and Coauthors, 2019: ACCESS-OM2: A global ocean-sea ice model at three resolutions. *Geosci. Model Dev. Discuss.*, https://doi.org/10.5194/gmd-2019-106.

Klinger, B. A., J. Marshall, and U. Send, 1996: Representation of convective plumes by vertical adjustment. *J. Geophys. Res.*, **101**, 18 175–18 182, https://doi.org/10.1029/96JC00861.

Kobayashi, S., and Coauthors, 2015: The JRA-55 Reanalysis: General specifications and basic characteristics. *J. Meteor. Soc. Japan*, **93**, 5–48, https://doi.org/10.2151/jmsj.2015-001.

Kuhlbrodt, T., and J. M. Gregory, 2012: Ocean heat uptake and its consequences for the magnitude of sea level rise and climate change. *Geophys. Res. Lett.*, **39**, L18608, https://doi.org/10.1029/2012GL052952.

——, A. Griesel, M. Montoya, A. Levermann, M. Hofmann, and S. Rahmstorf, 2007: On the driving processes of the Atlantic meridional overturning circulation. *Rev. Geophys.*, **45**, RG2001, https://doi.org/10.1029/2004RG000166.

——, J. M. Gregory, and L. C. Shaffrey, 2015: A process-based analysis of ocean heat uptake in an AOGCM with an eddy-permitting ocean component. *Climate Dyn.*, **45**, 3205–3226, https://doi.org/10.1007/s00382-015-2534-0.

Large, W. G., and S. G. Yeager, 2009: The global climatology of an interannually varying air–sea flux data set. *Climate Dyn.*, **33**, 341–364, https://doi.org/10.1007/s00382-008-0441-3.

——, J. C. McWilliams, and S. C. Doney, 1994: Oceanic vertical mixing—A review and a model with a nonlocal boundary-layer parameterization. *Rev. Geophys.*, **32**, 363–403, https://doi.org/10.1029/94RG01872.

Lee, H.-C., A. Rosati, and M. J. Spelman, 2006: Barotropic tidal mixing effects in a coupled climate model: Oceanic conditions in the northern Atlantic. *Ocean Modell.*, **11**, 464–477, https://doi.org/10.1016/j.ocemod.2005.03.003.

Le Quéré, C., and Coauthors, 2015: Global carbon budget 2015. *Earth Syst. Sci. Data*, **7**, 349–396, https://doi.org/10.5194/essd-7-349-2015.

Locarnini, R. A., and Coauthors, 2013: Temperature. Vol. 1, *World Ocean Atlas 2013*, NOAA Atlas NESDIS 73, 40 pp., http://data.nodc.noaa.gov/woa/WOA13/DOC/woa13_vol1.pdf.

Marshall, J., and T. Radko, 2003: Residual-mean solutions for the Antarctic Circumpolar Current and its associated overturning circulation. *J. Phys. Oceanogr.*, **33**, 2341–2354, https://doi.org/10.1175/1520-0485(2003)033<2341:RSFTAC>2.0.CO;2.

——, R. G. Williams, and A. J. G. Nurser, 1993: Inferring the subduction rate and period over the North Atlantic. *J. Phys. Oceanogr.*, **23**, 1315–1329, https://doi.org/10.1175/1520-0485(1993)023<1315:ITSRAP>2.0.CO;2.

Mashayek, A., R. Ferrari, G. Vettoretti, and W. R. Peltier, 2013: The role of the geothermal heat flux in driving the abyssal ocean circulation. *Geophys. Res. Lett.*, **40**, 3144–3149, https://doi.org/10.1002/grl.50640.

McCarthy, G., and Coauthors, 2015: Measuring the Atlantic meridional overturning circulation at 26°N. *Prog. Oceanogr.*, **130**, 91–111, https://doi.org/10.1016/j.pocean.2014.10.006.

McDougall, T. J., and R. Ferrari, 2017: Abyssal upwelling and downwelling driven by near-boundary mixing. *J. Phys. Oceanogr.*, **47**, 261–283, https://doi.org/10.1175/JPO-D-16-0082.1.

Megann, A., and Coauthors, 2014: GO5.0: The joint NERC-Met Office NEMO global ocean model for use in coupled and forced applications. *Geosci. Model Dev.*, **7**, 1069–1092, https://doi.org/10.5194/gmd-7-1069-2014.

Meinshausen, M., T. M. Wigley, and S. C. Raper, 2011: Emulating atmosphere-ocean and carbon cycle models with a simpler model, MAGICC6—Part 2: Applications. *Atmos. Chem. Phys.*, **11**, 1457–1471, https://doi.org/10.5194/acp-11-1457-2011.

Melet, A., S. Legg, and R. Hallberg, 2016: Climatic impacts of parameterized local and remote tidal mixing. *J. Climate*, **29**, 3473–3500, https://doi.org/10.1175/JCLI-D-15-0153.1.

Morrison, A. K., O. A. Saenko, A. M. Hogg, and P. Spence, 2013: The role of vertical eddy flux in Southern Ocean heat uptake. *Geophys. Res. Lett.*, **40**, 5445–5450, https://doi.org/10.1002/2013GL057706.

Munk, W. H., 1966: Abyssal recipes. *Deep-Sea Res.*, **13**, 707–730, https://doi.org/10.1016/0011-7471(66)90602-4.

Murray, R. J., 1996: Explicit generation of orthogonal grids for ocean models. *J. Comput. Phys.*, **126**, 251–273, https://doi.org/10.1006/jcph.1996.0136.

Otto, A., and Coauthors, 2013: Energy budget constraints on climate response. *Nat. Geosci.*, **6**, 415–416, https://doi.org/10.1038/ngeo1836.

Palter, J. B., S. M. Griffies, B. L. Samuels, E. D. Galbraith, A. Gnanadesikan, and A. Klocker, 2014: The deep ocean buoyancy budget and its temporal variability. *J. Climate*, **27**, 551–573, https://doi.org/10.1175/JCLI-D-13-00016.1.

Pellichero, V., J. B. Sallée, C. C. Chapman, and S. M. Downes, 2018: The Southern Ocean meridional overturning in the sea-ice sector is driven by freshwater fluxes. *Nat. Commun.*, **9**, 1789, https://doi.org/10.1038/s41467-018-04101-2.

Polzin, K. L., 1997: Ocean spatial variability of turbulent mixing in the abyssal ocean. *Science*, **276**, 93–96, https://doi.org/10.1126/science.276.5309.93.

Redi, M., 1982: Oceanic isopycnal mixing by coordinate rotation. *J. Phys. Oceanogr.*, **12**, 1154–1158, https://doi.org/10.1175/1520-0485(1982)012<1154:OIMBCR>2.0.CO;2.

Rhein, M., and Coauthors, 2013: Observations: Ocean. *Climate Change 2013: The Physical Science Basis*, T. F. Stocker et al., Eds., Cambridge University Press, 255–315.

Saenko, O. A., D. Yang, and J. M. Gregory, 2018: Impact of mesoscale eddy transfer on heat uptake in an eddy-parameterizing ocean model. *J. Climate*, **31**, 8589–8606, https://doi.org/10.1175/JCLI-D-18-0186.1.

Simmons, H. L., S. R. Jayne, L. C. Laurent, and A. J. Weaver, 2004: Tidally driven mixing in a numerical model of the ocean general circulation. *Ocean Modell.*, **6**, 245–263, https://doi.org/10.1016/S1463-5003(03)00011-8.

Snow, K., A. M. C. Hogg, S. M. Downes, B. M. Sloyan, M. L. Bates, and S. M. Griffies, 2015: Sensitivity of abyssal water masses to overflow parameterisations. *Ocean Modell.*, **89**, 84–103, https://doi.org/10.1016/j.ocemod.2015.03.004.

Solomon, H., 1971: On the representation of isentropic mixing in ocean models. *J. Phys. Oceanogr.*, **1**, 233–234, https://doi.org/10.1175/1520-0485(1971)001<0233:OTROIM>2.0.CO;2.

Stacey, M. W., S. Pond, and P. Nowak, 1995: A numerical model of the circulation in Knight Inlet, British Columbia, Canada. *J. Phys. Oceanogr.*, **25**, 1037–1062, https://doi.org/10.1175/1520-0485(1995)025<1037:ANMOTC>2.0.CO;2.

St. Laurent, L. C., J. M. Toole, and R. W. Schmitt, 2001: Buoyancy forcing by turbulence above rough topography in the abyssal Brazil basin. *J. Phys. Oceanogr.*, **31**, 3476–3495, https://doi.org/10.1175/1520-0485(2001)031<3476:BFBTAR>2.0.CO;2.

——, A. C. Naveira Garabato, J. R. Ledwell, A. M. Thurnherr, J. M. Toole, and A. J. Watson, 2012: Turbulence and diapycnal mixing in Drake Passage. *J. Phys. Oceanogr.*, **42**, 2143–2152, https://doi.org/10.1175/JPO-D-12-027.1.

Stommel, H., and A. B. Arons, 1960: On the abyssal circulation of the world ocean—II. An idealized model of the circulation pattern and amplitude in oceanic basins. *Deep-Sea Res.*, **6**, 140–154, https://doi.org/10.1016/0146-6313(59)90075-9.

Swift, J. H., 1984: The circulation of the Denmark Strait and Iceland-Scotland overflow waters in the North Atlantic. *Deep-Sea Res.*, **31A**, 1339–1355, https://doi.org/10.1016/0198-0149(84)90005-0.

Talley, L. D., and M. S. McCartney, 1982: Distribution and circulation of Labrador Sea water. *J. Phys. Oceanogr.*, **12**, 1189–1205, https://doi.org/10.1175/1520-0485(1982)012<1189:DACOLS>2.0.CO;2.

Tamsitt, V., L. D. Talley, M. R. Mazloff, and I. Cerovečki, 2016: Zonal variations in the Southern Ocean heat budget. *J. Climate*, **29**, 6563–6579, https://doi.org/10.1175/JCLI-D-15-0630.1.

——, R. P. Abernathey, M. R. Mazloff, J. Wang, and L. D. Talley, 2018: Transformation of deep water masses along Lagrangian upwelling pathways in the Southern Ocean. *J. Geophys. Res. Oceans*, **123**, 1994–2017, https://doi.org/10.1002/2017JC013409.

Tsujino, H., and Coauthors, 2018: JRA-55 based surface dataset for driving ocean–sea-ice models (JRA55-do). *Ocean Modell.*, **130**, 79–139, https://doi.org/10.1016/j.ocemod.2018.07.002.

Valcke, S., T. Craig, and L. Coquart, 2015: OASIS3-MCT User Guide. Tech. Rep., 54 pp., http://www.cerfacs.fr/oa4web/oasis3-mct_3.0/oasis3mct_UserGuide.pdf.

von Storch, J. S., H. Haak, E. Hertwig, and I. Fast, 2016: Vertical heat and salt fluxes due to resolved and parameterized mesoscale eddies. *Ocean Modell.*, **108**, 1–19, https://doi.org/10.1016/j.ocemod.2016.10.001.

Wolfe, C. L., P. Cessi, J. L. McClean, and M. E. Maltrud, 2008: Vertical heat transport in eddying ocean models. *Geophys. Res. Lett.*, **35**, L23605, https://doi.org/10.1029/2008GL036138.

Zika, J. D., W. P. Sijp, and M. H. England, 2013: Vertical heat transport by ocean circulation and the role of mechanical and haline forcing. *J. Phys. Oceanogr.*, **43**, 2095–2112, https://doi.org/10.1175/JPO-D-12-0179.1.

Zwally, H. J., and P. Gloersen, 1977: Passive microwave images of the polar regions and research applications. *Polar Rec.*, **18**, 431, https://doi.org/10.1017/S0032247400000930.

Zweng, M. M., and Coauthors, 2013: Salinity. Vol. 2, *World Ocean Atlas 2013*, NOAA Atlas NESDIS 74, 39 pp., http://data.nodc.noaa.gov/woa/WOA13/DOC/woa13_vol2.pdf.